Modelling Physics with Deep Learning: An Experimental Case of Cell Contractility

Yuanyuan Tao

Department of Electrical & Computer Engineering

McGill University

August, 2023

A thesis submitted to McGill University in partial fulfillment of the requirements of the degree of

Master of Science

Contents

Abstract

Deep Learning (DL) algorithms have been used to model physical systems. However, the success heavily relies on how DL methodologies accommodate the properties of a system and data. Especially for experimental data, noise and other confounding factors often significantly impede modeling and training. Under this context, we study the case of Traction Force Microscopy (TFM), a class of experimental procedures and algorithms for measuring cell traction. While TFM has contributed to numerous discoveries over the past three decades, its application has been limited due to demanding experimental requirements and the ill-posed inverse problem of computing cell traction from substrate displacement. To address these challenges, we introduce Deep Morphology Traction Microscopy (DeepMorphoTM), a DL approach that infers cell traction from a shape sequence of a cell. By employing a deterministic framework, DeepMorphoTM effectively mitigates the biological variability in cell contractility for a given cell shape. Leveraging the smoothness of Neural Network (NN) output, DeepMorphoTM directly infers the displacement and then computes the traction, circumventing the ill-posedness in training

and inference. Moreover, alternative model designs and accurate extrapolation across cell types and substrate materials provide additional insights into the cellular system, revealing information beyond TFM analysis. Apart from establishing new avenues for investigating cell mechanics, this study sets an excellent example of modeling and studying physical systems with DL from experimental data.

Résumé

Les algorithmes d'apprentissage profond (DL) ont été utilisés pour modéliser des systèmes physiques. Cependant, le succès dépend fortement de la manière dont les méthodologies DL prennent en compte les propriétés d'un système et des données. En particulier pour les données expérimentales, le bruit et d'autres facteurs de confusion entravent souvent de manière significative la modélisation et l'apprentissage. Dans ce contexte, nous étudions le cas de la microscopie à force de traction (TFM), une classe de procédures expérimentales et d'algorithmes pour mesurer la traction cellulaire. Bien que la TFM ait contribué à de nombreuses découvertes au cours des trois dernières décennies, son application a été limitée en raison des exigences expérimentales élevées et du problème inverse mal posé du calcul de la traction cellulaire à partir du déplacement du substrat. Pour relever ces défis, nous présentons Deep Morphology Traction Microscopy (DeepMorphoTM), une approche DL qui déduit la traction cellulaire à partir d'une séquence de formes d'une cellule. En utilisant un cadre déterministe, DeepMorphoTM atténue efficacement la variabilité biologique de la contractilité cellulaire pour une forme de cellule donnée. En tirant parti de la douceur des

sorties des réseaux neuronaux (NN), DeepMorphoTM déduit directement le déplacement et calcule ensuite la traction, ce qui permet de contourner les problèmes d'apprentissage et d'inférence. En outre, les modèles alternatifs et l'extrapolation précise à travers les types de cellules et les matériaux de substrat fournissent des informations supplémentaires sur le système cellulaire, révélant des informations au-delà de l'analyse TFM. Outre le fait qu'elle ouvre de nouvelles voies pour l'étude de la mécanique cellulaire, cette étude constitue un excellent exemple de modélisation et d'étude de systèmes physiques à l'aide de DL à partir de données expérimentales.

To My Parents

Acknowledgements

I first express my deepest gratitude to Dr. Allen Ehrlicher. For the past five years, Allen's mentorship has been instrumental to my academic and personal growth. Through his distinct view on problems, Allen consistently challenges and reshapes my way of thinking. With great patience, Allen has led me through my first project, first research, and first publication. Whenever I need extra help, Allen always generously provides me with the best resources and opportunities. To me as a young adult, the past five years of life has been confusing and sometimes challenging, but Allen has always been there for me and gradually shaped me into a better person by teaching and showing me honesty, empathy, and responsibility.

I would like to most sincerely thank Dr. Derek Nowrouzezahrai for his pivotal role at the turning point of my academic and professional path. As I was just delving into machine learning, computer graphics, and physics simulation, Derek laid a solid foundation for me to build upon with his expertise, insights, and guidance. While fostering a meticulous and effective research methodology, Derek leads me through projects and supports my ideas and interests, cordially helping me with problems of any magnitude. I am profoundly grateful

for his indispensable efforts that have shaped and will continue to shape my new career trajectory.

I extend my utmost appreciation to Dr. Paul Kry for steering me through my first project in my new career direction. Paul is always eager to help and hopeful, supporting me through challenging times of the project. His encouragement and guidance empowers me to accomplish tasks that I would believe to be impossible. His insights and vision propel me forward when I am lost. I am honoured and excited to embark on my future journey with Paul.

My study and this thesis would not have been completed without the crucial contributions and support from my coauthors, collaborators, and friends. I cannot appreciate Amy Ji enough for being incredibly generous and caring to me. During this academic and professional journey, Amy has been the anchor of my life, and her help always reaches wherever it is needed, including editing the thesis and reviewing Traction Force Microscopy. I also thank Clayton Molter for studying and reviewing Traction Force Microscopy with me, and the coauthors and collaborators for their work in the manuscript.

I am grateful to all my colleagues, friends, and labs. My first lab, the Ehrlicher lab has been a nurturing home. I work and became friends with wonderful people here – Pouria, Clayton, Ajinkya, Cameron, Anna, Amy, Haruka, Luv, LP, Ali, Adele, Johanan, and Newsha. When I joined the lab, Pouria taught me everything. We did so many awesome, stupid, and fun things together and became best friends. Pouria has supported me in life and work and

I would have had a different life and career otherwise. My second lab, the McGill Graphics and Imaging Lab comprises a remarkable community of talented, dedicated, and generous people. I express my heartfelt gratitude to Sayantan, Mattie, Joey, and Loren for their help along the way of my study. Finally, I thank my internship team, Ivan, Yangyang, Xinhao, Manas, and Andrei, for the great experience at the start of my new career. I am indebted to Ivan for patiently teaching me everything to start my new career and enthusiastically solving challenges in my project with me.

There is no way to thank my family and dearest friends enough for their dedication to me. Their consistent support, protection, and companionship get me through the toughest times and make the person who I am today. If you are reading - you hold the deepest and most cherished place in my heart.

Contribution of Authors

Chapter 2. Inferring Cellular Contractile Forces and Work using Deep Morphology Traction Microscopy

Yuanyuan Tao, Ajinkya Ghagre, Anna Clouvel, Jalal Al Rahbani, Claire M. Brown, Clayton W. Molter, Derek Nowrouzezahrai, Allen J. Ehrlicher

First author, Yuanyuan Tao, conceptualized the project, developed and implemented the methodology and algorithms, and wrote the manuscript.

Conceptualization: A.J.E., Y.T.; Methodology development: Y.T., A.G., A.C.; Methodology application: Y.T.; Image Data Acquisition: A.C., C.W.M., J.A.R.; Investigation: A.G.; Software: Y.T.; Writing original draft: Y.T., A.G.; Review and editing: Y.T., A.G., A.J.E., C.M.B.; Funding acquisition: A.J.E.; Resources: A.J.E; Supervision: A.J.E., D.N.

List of Figures

List of Acronyms

BEM	Boundary Element Method.
CNN	Convolutional Neural Network.
DeepMorphoTM	Deep Morphology Traction Microscopy.
DL	Deep Learning.
FEA	Finite Element Analysis.
FT	Fourier Transform.
FTTC	Fourier Transform Traction Cytometry.
NN	Neural Network.
PIV	Particle Image Velocimetry.
RMSD	Root Mean Squared Displacement.
RMST	Root Mean Squared Traction.
RNN	Recurrent Neural Network.
SDF	Signed Distance Function.
SVD	Singular Value Decomposition.

TFM	Traction Force Microscopy.
wAD	weighted Angle Deviation.
wAND	weighted Absolute Norm Deviation.
wNPC	weighted Norm Pearson Correlation.
wVD	weighted Vector Deviation.

Chapter 1

Introduction

This thesis explores modeling a physical system with Deep Learning (DL) by investigating the experimental case of cell contractility. The goal is to develop a DL approach that infers cell traction from experimentally measured cell shapes. This approach offers a simpler and more robust alternative to the current method for measuring cell traction, Traction Force Microscopy (TFM). Challenges faced by TFM are addressed by this approach. The mathematics, mechanics, biology, and algorithms behind TFM and cell contractility are studied. The outcomes of this approach and their implications are interpreted in the context of this approach and modeling physics with DL in general.

1.1 Thesis organization

This manuscript-based thesis comprises four chapters. Chapter 1 provides an overview of the thesis and enters the case study from the angle of TFM. Chapter 2 is the manuscript in which a DL approach modeling cell contractility is developed. Chapter 3 further discusses the mathematics, mechanics, and algorithms behind the system of a cell and its underlying substrate, the properties of the system and data, and their impact on the design of DL methodologies. Chapter 4 concludes the thesis and suggests future directions.

1.2 Traction Force Microscopy

Cell contractility is essential in a wide array of biological processes such as differentiation [Yim and Sheetz 2012] and tissue development [DuFort et al. 2011], as well as homeostatic functions including wound healing [Li and Wang 2011], heart contraction [Münch and Abdelilah-Seyfried 2021; Pasqualini et al. 2018], and cell division [Lesman et al. 2014; Taneja et al. 2019]. Moreover, abnormal contractile phenotypes appear in an ever-expanding array of diseases, such as cancer [Kumar and Weaver 2009] and asthma [Berair et al. 2013; Ram-Mohan et al. 2020]. In addition to being a potential biomarker for various diseases, contractility is also a key factor mediating other well-recognized mechanobiological processes, including stretch-activated ion channels [Ellefsen et al. 2019], nucleus-mediated mechanotransduction [Elosegui-Artola et al. 2017], modulation of cell

stiffness [Chowdhury et al. 2021], and extracellular matrix rigidity sensing [Doss et al. 2020; Yim and Sheetz 2012]. Given the clear importance of cell contractility in physiology and pathology, this has driven an explosion of innovative methods to quantify these forces in different contexts. Particularly, cell traction forces - the mechanical interactions between cells and their underlying substrate - have been widely accepted as a metric to quantify cell contractility. Traction forces were first observed on and calculated from the wrinkling of thin, silicone rubber films [Harris et al. 1980; Lee et al. 1994]. This method lacked precision due to topography changes during wrinkling and inconsistencies in said films sticking or slipping. Later, silicone micropost arrays were employed to calculate traction forces from the bending of cell-actuated microposts [Tan et al. 2003]. This approach also presents limitations including a prescribed adhesion area and cell-induced substrate deformations being limited by the bending limit of the microposts. Additionally, no force is transmitted through the discrete micropost array.

The current gold-standard biophysical technique used to quantify cell contractility is TFM. In brief, TFM generally quantifies traction stress exerted by cells on their surroundings by measuring cell-induced deformations on continuous substrates of known stiffness. Substrate deformations can be readily obtained as a displacement vector field by applying cross-correlation algorithms, such as Particle Image Velocimetry (PIV), on paired images of the substrate with and without the deformations [Adrian 1984; Keane and Adrian 1993; Raffel et al. 1998; Stamhuis and Videler 1995; Willert and Gharib 1991].

Typically in TFM, cells crawl on 2D substrates. This setting makes a 2D in-plane displacement field sufficient to recover in-plane traction stresses, providing a convenient solution in terms of experimental complexity and compatibility with lab-standard microscope imaging. Over the last three decades, a variety of TFM algorithms have been developed to solve the problem globally or locally. The global approach addresses the vector fields of traction and displacement. Often, the Green's function, which defines the relationship between the vector fields, is used. In 1999, Dembo and Wang initially solved the traction on a mesh over the cell area by Boundary Element Method (BEM) with Bayesian likelihood [Dembo and Wang 1999]. In 2001, Balaban et al. used Singular Value Decomposition (SVD) without a mesh [Balaban et al. 2001; Schwarz et al. 2002]. Around the same time, Butler et al. proposed Fourier Transform Traction Cytometry (FTTC) that significantly reduced the computational cost by taking the Fourier Transform (FT) of the entire problem and solving the problem in the frequency domain [Butler et al. 2002]. Taking the global approach without the Green's function, in 2009, Hur et al. calculated the traction by Finite Element Analysis (FEA) [Hur et al. 2009, 2012]. Alternatively in a local view, by considering only the constitutive relation between strain and stress, rather than the vector fields, the calculation was done with 3D displacement [Maskarinec et al. 2009; Toyjanova et al. 2014].

Although TFM has been implemented with a diversity of methods, the vast majority of the algorithms take the global approach and share a common fundamental challenge: the

"ill-posed" inverse problem of calculating the traction vector field from the cell-induced substrate displacement vector field. Problematically, the calculation is extremely sensitive to noise in the displacement data, which is an intrinsic property of the ill-posed problem. To mitigate potential noise-generated error, regularization has been added to the traction computation [Brask et al. 2015; Colin-York et al. 2016; Han et al. 2015; Huang et al. 2019; Legant et al. 2010; Sabass et al. 2008; Schwarz et al. 2002; Suñe-Auñón et al. 2016, 2017; Tanimoto and Sano 2012; Tikhonov et al. 1995]. Instead of an exact solution accounting for both the actual displacement and the noise, regularization promotes a solution corresponding to a "more regular" or "simpler" part of the displacement data based on assumptions about the problem, as opposed to the "irregular" or "complex" contribution of the noise. Reasonably, the nature and amount of the applied simplification or "regularity" could significantly affect the result. Therefore, regardless of the algorithm, the fundamental challenge of using TFM lies in the application of the appropriate noise-management strategy – specifically, the regularization and associated parameters. The selection of the strategy depends on specific experimental condition and requires additional expertise in math and computer science. Accordingly, while the noise-management strategies continue to be proposed for improving TFM practices, these improved techniques are seldomly implemented to their full effect across the TFM community where to date the choice of strategy can still be somewhat arbitrary, thus impairing quantitative reproducibility across different studies [Brask et al. 2015; Colin-York et al. 2016; Han et al. 2015; Huang et al.

2019; Legant et al. 2010; Sabass et al. 2008; Schwarz et al. 2002; Suñe-Auñón et al. 2016, 2017; Tanimoto and Sano 2012]. A lack of standardized implementation of TFM creates major obstacles in the advancement of cell force studies and general mechanobiology.

Despite the importance of technique fundamentals, the mathematical components of TFM and its associated noise-management techniques are often only superficially discussed in papers that adopt them for their analysis. This drift in descriptive rigor has progressively obscured the functional consequences that certain analysis decisions may entail. Even in existing TFM review articles, the math components and noise management are often presented in an inaccessible mathematical level or without enough context for the reader to make informed alterations to their TFM workflow. In pursuit of an optimized and perhaps standardized implementation of TFM that will support increasing mechanobiology studies, there is a growing need for increased literacy among TFM users for the technique more than ever. Therefore, the mechanical and mathematical core of TFM is explained by this thesis in an intuitive fashion. The goal is to enable users to discern the functional outcomes or pitfalls of the various TFM implementations seen throughout literature and to provide insight on best practices of TFM.

1.2.1 The mechanics behind TFM

In crawling cell motility, a cell adheres to and pulls the underlying substrate via focal adhesions. In TFM, while the cell usually crawls on the 2D flat surface of the substrate,

the pulling exerts 3D force, creating stress and deformation throughout the substrate. The stress and deformation follow two rules. First, because the acceleration of the cell is small enough to be ignored, the substrate is assumed to be in mechanical equilibrium where forces are balanced throughout. The stress can be considered to balance everywhere in the substrate, as described by the divergence of the stress tensor:

$$\rho\boldsymbol{\alpha} = \frac{d\mathbf{F}}{dV} = \nabla \cdot \boldsymbol{\sigma} = \begin{bmatrix} \frac{\partial \sigma_{11}}{\partial x_1} + \frac{\partial \sigma_{21}}{\partial x_2} + \frac{\partial \sigma_{31}}{\partial x_3} \\ \frac{\partial \sigma_{12}}{\partial x_1} + \frac{\partial \sigma_{22}}{\partial x_2} + \frac{\partial \sigma_{32}}{\partial x_3} \\ \frac{\partial \sigma_{13}}{\partial x_1} + \frac{\partial \sigma_{23}}{\partial x_2} + \frac{\partial \sigma_{33}}{\partial x_3} \end{bmatrix} = \mathbf{0} \tag{1.1}$$

where ρ is the density of the substrate; $\boldsymbol{\alpha}$ is the acceleration of a point in the substrate; $\mathbf{F}$ is the force at a point in the substrate; V denotes volume; σ_{ij} is a stress component, that resides on dimension x_i and is parallel with axis x_j, of a stress tensor $\boldsymbol{\sigma}$ (Fig. 1.1). Second, the stress and deformation are bound by the constitutive relation of the material of the substrate. This relationship resembles the relation between force and displacement of a linear spring under compression or extension, as described by Hooke's law $F = kx$. In experiments, the substrate, often a continuous isotropic linearly elastic material, follows a

similar relation, generalized from Hooke's Law:

$$\boldsymbol{\sigma} = \begin{bmatrix} \sigma_{11} \\ \sigma_{22} \\ \sigma_{33} \\ \sigma_{23} \\ \sigma_{13} \\ \sigma_{12} \end{bmatrix} = \mathbf{C}\boldsymbol{\varepsilon} = \frac{E}{(1+\nu)(1-2\nu)} \begin{bmatrix} 1-\nu & \nu & \nu & 0 & 0 & 0 \\ \nu & 1-\nu & \nu & 0 & 0 & 0 \\ \nu & \nu & 1-\nu & 0 & 0 & 0 \\ 0 & 0 & 0 & \frac{1-2\nu}{2} & 0 & 0 \\ 0 & 0 & 0 & 0 & \frac{1-2\nu}{2} & 0 \\ 0 & 0 & 0 & 0 & 0 & \frac{1-2\nu}{2} \end{bmatrix} \begin{bmatrix} \varepsilon_{11} \\ \varepsilon_{22} \\ \varepsilon_{33} \\ 2\varepsilon_{23} \\ 2\varepsilon_{13} \\ 2\varepsilon_{12} \end{bmatrix} \tag{1.2}$$

where $\boldsymbol{\varepsilon}$ is a strain tensor, constructed in the same way as $\boldsymbol{\sigma}$ (Fig. 1.1); $\mathbf{C}$ is a stiffness tensor. Strain, a measure of deformation, is related to the gradient of the displacement. The stiffness tensor $\mathbf{C}$ defines the material properties of the substrate and maps the strain tensor to the stress tensor.

The stress on the surface is traction:

$$\mathbf{T} = \begin{bmatrix} T_1 \\ T_2 \\ T_3 \end{bmatrix} = \boldsymbol{\sigma}\mathbf{n} = \begin{bmatrix} \sigma_{11} & \sigma_{21} & \sigma_{31} \\ \sigma_{12} & \sigma_{22} & \sigma_{32} \\ \sigma_{13} & \sigma_{23} & \sigma_{33} \end{bmatrix} \begin{bmatrix} n_1 \\ n_2 \\ n_3 \end{bmatrix} \tag{1.3}$$

where $\mathbf{T}$ is a traction vector and $\mathbf{n}$ is an outward unit normal vector to the surface of the substrate. In the case of a 2D substrate, $\mathbf{n} = [0\ 0\ 1]'$ is the out-of-plane direction. As the surface not in contact with the focal adhesions is free, the traction vector field is only non-

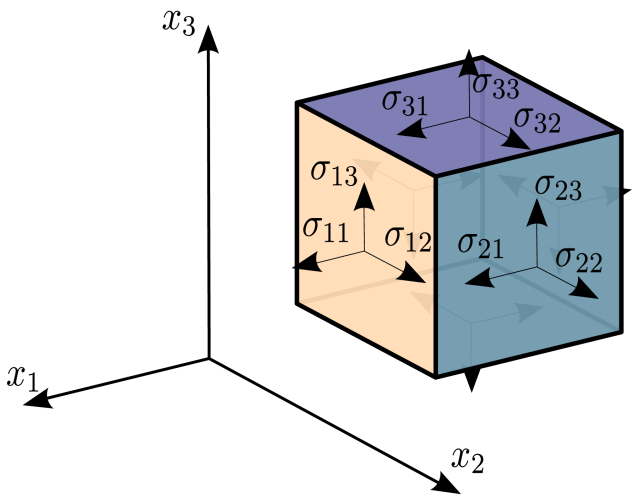

Figure 1.1: A stress tensor fully defines the state of stress at a point. σ_{ij}, a component of a stress tensor, is on dimension x_i and along axis x_j.

zero at the focal adhesions. Importantly, non-zero traction at any location contributes to the deformation throughout the entire substrate, with the degree of contribution depending on factors such as the material properties of the substrate and the relative location of the traction. In other words, while the tractions are spatially discrete, the displacement of the substrate at any location is a function of the entire traction field. The relation between the traction and displacement is linear and can be written in the form of a convolution or Fredholm integral equation of the first kind:

$$\mathbf{u}(\mathbf{r}) = (\mathbf{G} * \mathbf{T})(\mathbf{r}) = \int \mathbf{G}(\mathbf{r} - \mathbf{r}')\mathbf{T}(\mathbf{r}')\, d\mathbf{r}' \tag{1.4}$$

where $\mathbf{u}(\mathbf{r})$ is a displacement vector at a point $\mathbf{r}$ on the interface; $\mathbf{T}(\mathbf{r}')$ is the traction vector at a point $\mathbf{r}'$; $\mathbf{G}$ is a Green's function or Green's tensor (Fig. 1.2).

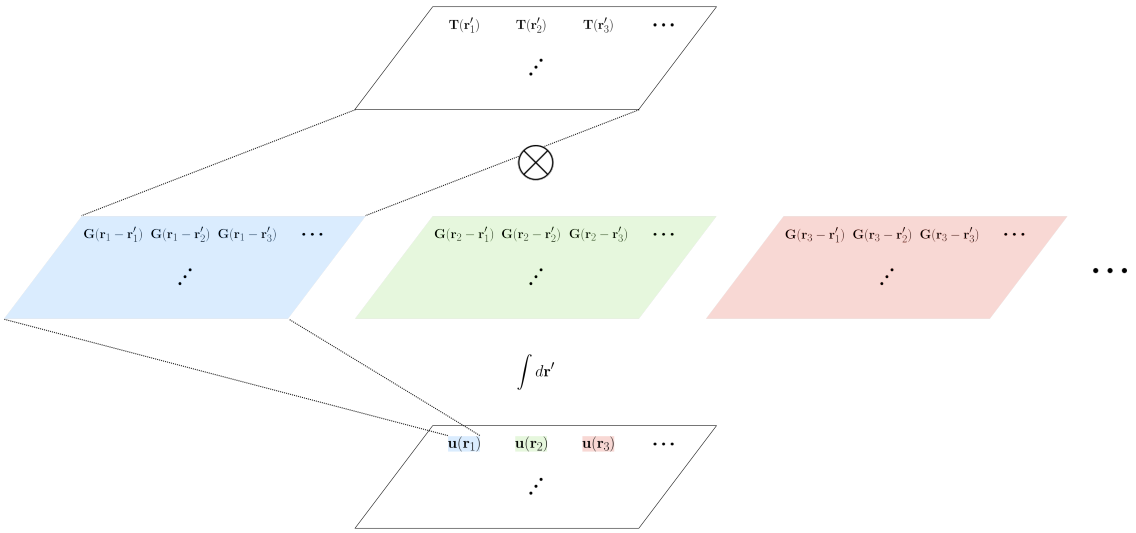

Figure 1.2: The relationship between traction and displacement is defined by a Fredholm integral equation of the first kind. $\mathbf{r}_i$ and $\mathbf{r}'_j$ are points in the vector fields.

G serves as a linear map from **T** to **u** and defines the relation between the displacement and traction. Therefore, the Green's function depends on the experimental setups, incorporating factors such as the topography, thickness, linearity, and the (an)isotropy of the substrate. Given such conditions, the function can be derived with the constitutive relation of the substrate material and Eq. (1.1) [Landau and Lifshitz 1986]. Particularly for elastic substrates under small deformation, the Green's function can be derived through the theory of elasticity, with Eq. (1.1) and (1.2), and boundary conditions such as zero force or displacement on the bottom and sides of the substrate [Landau and Lifshitz 1986]. Most commonly, TFM experiments use "ideal" substrates that are flat, thick, homogeneous, isotropic, and linearly elastic. In this case, the Green's function is the solution of the Boussinesq problem, i.e. the stress in an isotropic linearly elastic half-space

under a point-source load [Boussinesq 1885; Landau and Lifshitz 1986; Schwarz et al. 2002]. Although the out-of-plane stress has been shown to be significant in some cases, the out-of-plane traction and displacement are often ignored [Brask et al. 2015; Butler et al. 2002; Dembo and Wang 1999; Huang et al. 2009; Hur et al. 2009, 2012; Notbohm et al. 2012; Sabass et al. 2008; Schwarz and Soiné 2015]. By neglecting the out-of-plane components and thus reducing $\mathbf{T}$ and $\mathbf{u}$ to 2D vector fields, the Green's function for this standard TFM experimental condition is accordingly reduced to this 2D function:

$$\mathbf{G}_{\text{in-plane}}(\mathbf{r}) = \frac{1+\nu}{\pi E r^3} \begin{pmatrix} (1-\nu)r^2 + \nu r_{x_1}^2 & \nu r_{x_1} r_{x_2} \\ \nu r_{x_1} r_{x_2} & (1-\nu)r^2 + \nu r_{x_2}^2 \end{pmatrix} \tag{1.5}$$

where $\mathbf{r} = (r_{x_1}, r_{x_2})$ and $r = \sqrt{r_{x_1}^2 + r_{x_2}^2}$ is the distance from the origin to $\mathbf{r}$; ν is the Poisson ratio; E is Young's modulus. In Eq. (1.4), $\mathbf{r} - \mathbf{r}'$ in $\mathbf{G}(\mathbf{r} - \mathbf{r}')$ is the relative location of $\mathbf{r}$ to $\mathbf{r}'$. Noticeably, $\mathbf{G}_{\text{in-plane}}$ spatially decays by a factor of $\frac{1}{r}$, making the displacement resulting from a point traction also decay by a factor of $\frac{1}{r}$.

Eq. (1.4) shows the causal process of the interaction between the traction and displacement and defines the forward problem: $\mathbf{u}(\mathbf{r})$ at any point $\mathbf{r}$ combines all the information from the entire field of $\mathbf{T}$ through the integration with $\mathbf{G}$. However, TFM addresses the inverse problem that $\mathbf{T}$ needs to be calculated from $\mathbf{u}$ through $\mathbf{G}$.

1.2.2 Strategies employed by TFM algorithms

TFM algorithms attempt the problem with either a global or a local view. In the global view, the Green's function maps the traction field to the displacement field, so Eq. (1.4) needs to be inverted to calculate the traction. This inversion creates a notorious ill-posed inverse problem. In the local view, the ill-posed inverse problem is avoided, but additional data needs to be acquired and processed, requiring less accessible experiments and computational resources. Generally, TFM algorithms take one of three strategies, two of which take the global view.

First, globally, with a Green's function, Eq. (1.4) can be inverted. As one of the first attempts employing this approach, the inverse problem was solved using BEM with Bayesian likelihood [Dembo and Wang 1999]. Later, SVD was employed with L^2 regularization and optionally the location of focal adhesions to handle the ill-posedness [Balaban et al. 2001; Schwarz et al. 2002]. A discretized 2D Green's function is a 2D matrix. Because the Green's function decays slowly, the function results in a very large matrix for every point in the displacement field. With the size of the displacement field, every matrix must be inverted to solve the traction, making the calculation computationally expensive and slow [Butler et al. 2002]. This computational challenge, however, can be resolved via an FT approach: the convolutional equation in real space becomes multiplication in Fourier space, annulling the need for the inversion of large matrices, leading to a new computationally efficient approach, FTTC [Butler et al. 2002]. While in the original implementation FTTC did not include

regularization due to the ideal data used, regularization is necessary in many cases and can be applied in the Fourier domain [Suñe-Auñón et al. 2017].

Second, still globally, when the Green's function is not known, the same linear system described by Eq. (1.4) can be solved as a boundary value problem by FEA, following Eq. (1.1), (1.2), and (1.3). By using the surface displacement and the assumption of zero-stress beyond the region of interest as boundary conditions, along with the substrate material properties, the stress distribution in the entire substrate can be calculated [Hur et al. 2009, 2012]. As this approach still solves the same inverse problem, the ill-posedness is still implicitly faced. Moreover, due to the technical complexity of FEA, this approach is more difficult to implement. In addition to solving entirely with FEA, hybrid methods can use FEA to calculate the unknown Green's function and then with the Green's function in hand, methods in the first strategies, such as SVD with L^2 regularization, can be used to calculate the traction [Legant et al. 2010].

Finally, the third approach takes the local view by using Eq. (1.2), a 3D displacement field, and Hooke's law for small strain or Neo-Hookean model for large strain [Maskarinec et al. 2009; Toyjanova et al. 2014]. As the approach only deals with the local constitutive relation, the ill-posed inverse problem is circumvented, and the computation is trivial. Nevertheless, a 3D displacement field for depth near the surface of the substrate must be measured to calculate the strain tensors, making this approach experimentally challenging and computationally intensive [Maskarinec et al. 2009; Toyjanova et al. 2014]. Thus, this

technique is relatively less common throughout literature compared to solving the ill-posed inverse problem.

In summary, the FTTC approach is currently the fastest and easiest to use, but only limited to experimental settings with known Green's function, whereas the rest are slower and require more expertise to use, but are flexible for different experimental settings.

Chapter 2

Inferring Cellular Contractile Forces and Work using Deep Morphology Traction Microscopy

Submitted to Biophysical Journal.

Yuanyuan Tao[1,9], Ajinkya Ghagre[1], Anna Clouvel[1], Jalal Al Rahbani[7], Claire M. Brown[2,7,8], Clayton W. Molter[1], Derek Nowrouzezahrai[9], Allen J. Ehrlicher[1,2,3,4,5,6]*

[1] Department of Bioengineering, McGill University, Montreal, Canada

[2] Department of Anatomy and Cell Biology, McGill University, Montreal, Canada

[3] Department of Biomedical Engineering, McGill University, Montreal, Canada

[4] Department of Mechanical Engineering, McGill University, Montreal, Canada

[5] Rosalind and Morris Goodman Cancer Research Institute, McGill University, Montreal, Canada

[6] Centre for Structural Biology, McGill University, Montreal, Canada

[7] Department of Physiology, McGill University, Montreal, Canada

[8] Advanced BioImaging Facility (ABIF), McGill University, Montreal, Canada

[9] Department of Electrical and Computer Engineering, McGill University, Montreal, Canada

**Lead Contact: allen.ehrlicher@mcgill.ca (AJE)*

2.1 Abstract

Traction Force Microscopy (TFM) has emerged as a broadly applicable standard methodology to measure cell-generated traction forces and their role in regulating cell behavior. While TFM platforms have enabled many discoveries, their implementation remains limited due to complex experimental procedures, specialized substrates, and the ill-posed inverse problem where small high-frequency noise in the displacement severely contaminates the traction. Here, we introduce Deep Morphology Traction Microscopy (DeepMorphoTM), a Deep Learning (DL) alternative to quantify cell-generated traction forces directly from the cell shape. DeepMorphoTM first infers cell-induced substrate displacement solely from a shape sequence of a cell and subsequently computes cellular

traction forces, thus avoiding the requirement of a specialized deformable fiduciary marked substrate and simplifying the overall methodology, imaging, and analysis. We demonstrate that DeepMorphoTM matches conventional TFM in result, while offering stability against the biological variability in cell contractility for a given cell shape. As such, the inference reduces variance in the quantification of cell contractility and potentially the need of experimental replication. Without high-frequency noise in the inferred displacement, DeepMorphoTM also resolves the ill-posedness of traction computation, increasing the consistency and accuracy of traction analysis. Moreover, the accurate extrapolation across cell types and substrate materials suggests robustness of the methodology. Accordingly, we present DeepMorphoTM as a robust yet simpler alternative to conventional TFM for characterizing cellular contractility in 2D.

2.2 Statement of significance

Traction force microscopy has served as a gold standard for cell traction force measurement in the field of mechanobiology. However, its experimental and analytical complications have made its translation difficult in settings outside of specialized biophysics labs. DeepMorphoTM, a readily implemented alternative, uses deep learning to accurately infers cell-generated displacement and traction directly from a shape sequence of a cell. This approach demonstrates stability against the biological viability in cell contractility for a given cell shape, reducing variance in contractility analysis. The inferred displacement is

also free from high-frequency noise that plagues the computation of traction, yielding stable and consistent traction quantification. DeepMorphoTM applies accurately across cell types and substrate materials, suggesting common mechanics of cell contractility and robustness of the methodology.

2.3 Introduction

Cells are sensitive to the mechanics imposed by their surrounding microenvironment. Cells recognize microenvironment mechanical cues using traction forces generated by actomyosin, and respond biologically in forms such as cell proliferation [Petridou et al. 2017], directed migration [Ladoux and Mégé 2017; Van Helvert et al. 2018], and differentiation [Engler et al. 2006; Vining and Mooney 2017]. Correct recognition and transduction of such mechanical cues are essential to health whereas defective responses are associated with diseases such as cancer [Ingber 2003; Jaalouk and Lammerding 2009]. Hence it is critical to quantify cell traction forces to understand how cells recognize and react to microenvironment mechanics, as this measurement may open new avenues for disease diagnosis and specialized therapies.

Traction Force Microscopy (TFM) is a widely used technique for measuring cell traction forces. TFM has characterized the roles of cell traction forces in regulating diverse physiological and pathological processes in virtually all adherent cells, thus making traction force measurements a critical aspect of studying biological behaviors and identifying pathologies [Rokhzan et al. 2019; Wheelwright et al. 2018; Yoshie et al. 2018, 2019]. Useful

as TFM is, its exploitation and implementation are limited by its own complexity. TFM often utilizes protein-functionalized elastic substrates, often silicone or polyacrylamide, containing submicrometer fluorescent beads acting as fiduciary markers to capture cell-induced substrate deformations. A typical TFM experiment involves imaging the substrate beads in the cell-contractile state, followed by the detachment of cells to image the beads again to determine their positions in the unstressed state. The resulting two images are analyzed to generate a displacement vector field, which along with known mechanical properties of the substrates are used to calculate traction forces and cell strain energy based on the theory of elasticity [Dembo et al. 1996; Butler et al. 2002; Dembo and Wang 1999; Hur et al. 2009; Toyjanova et al. 2014].

Although TFM provides traction force measurements, a substantial complication in many but not all [Banda et al. 2019; Bergert et al. 2016; Fu et al. 2010; Ghagre et al. 2021; Ghassemi et al. 2012; Park et al. 2015; Plotnikov et al. 2012; Balaban et al. 2001; Tan et al. 2003] forms of this technique is the necessity to acquire a "null force" reference image to quantify cell-induced bead displacements and subsequent traction force measurements. This markedly complicates experimental procedures, imaging, and analysis, and it precludes cellular postprocessing, such as immunofluorescence staining. Furthermore, the calculation of the traction forces from the substrate displacements has also been a fundamental challenge. Over almost three decades, a diverse variety of TFM algorithms have been proposed, with the common approach calculating each traction vector from the

entire displacement vector field [Dembo et al. 1996; Balaban et al. 2001; Butler et al. 2002; Dembo and Wang 1999; Hur et al. 2009; Lee et al. 1994; Legant et al. 2010]. However, all these approaches face the notorious ill-posed inverse problem in which the computation of traction is extremely unstable. Small but high-frequency noise in the experimentally measured displacement is amplified to significant perturbation in the traction, requiring nontrivial measures to attempt stability [Brask et al. 2015; Huang et al. 2019; Schwarz et al. 2002; Suñe-Auñón et al. 2017]. Alternatively, the traction can be calculated from local strain tensors, which is a function of displacement gradient. Yet, leveraging the constitutive relation between strain and stress requires three-dimensional displacement that is difficult to acquire experimentally [Maskarinec et al. 2009; Toyjanova et al. 2014]. Thus, the complex experimental procedure and computational drawbacks of TFM call for a more streamlined and robust method to quantify cell traction forces.

From a material perspective, every cell and the underlying substrate is a mechanical system obeying the laws of physics, including the conservation of momentum and constitutive relations. Each component of the system possesses distinctive properties, sustains loads, and contributes to cell deformation that ultimately manifests in the cell shape. The shape of adherent cells is closely related to actin-cytoskeletal structure, cell traction, and biological processes [Murrell et al. 2015; Oakes et al. 2014; Rape et al. 2011; Tan et al. 2003]. For instance, many cells, when allowed to adhere and spread in 2D without constraints, often reach an extended polygonal shape and form long and thick

actin filaments, accompanied with increased traction forces. Irrespective of cell area, cells with sharp vertices have been shown to apply large traction forces at vertices that effect biological responses such as differentiation [Oakes et al. 2014; Rape et al. 2011; Tan et al. 2003]. Recently, analytical models have been proposed to calculate the traction forces from the shape of a cell. For example, Oakes et al. modelled the cell as a thin homogeneous and isotropic elastic film with line tension and homogeneous contractile pressure, and adhesions as a uniform distribution of linear springs [Oakes et al. 2014]. Assuming mechanical equilibrium, the force-balance model of the system is obtained by the principle of minimum energy. Given the cell shape and properties of the system, the traction is calculated. However, such analytical models depend on the detailed knowledge and unrealistic assumption of the experimental system, lacking magnitude of traction and generalizability. In this way, it is not possible to infer traction forces using cell shape alone.

Deep Learning (DL) algorithms are often used to learn complex parametrized models from data. Recently, the downstream problem of computing the traction from deformed substrate has been attempted with Deep Learning (DL) [Duan and Huang 2022; Wang and Lin 2021]. However, the learning algorithms can directly extract and exploit spatiotemporal features from the cell shape sequences to approximate the mechanics of cell traction. In particular, Convolutional Neural Networks (CNNs) excel at extracting local invariant features from structured spatiotemporal data such as the shape of cell [LeCun et al. 1989]. One of the most popular CNN architectures, U-Net, highlights the precise localization and high resolution in

the construction of the output, making this design ideal for inferring field data for the cell and substate [Ronneberger et al. 2015].

Here, we demonstrate Deep Morphology Traction Microscopy (DeepMorphoTM), a Deep Learning (DL) approach that infers cell traction force solely from a shape sequence of a cell, resulting in a stable, consistent, accurate, and dramatically simpler alternative to TFM, without introducing additional experimental procedure or analysis. Examined under a comprehensive set of metrics, DeepMorphoTM establishes the competence of Deep Learning (DL) in modelling cell mechanics and inferring mechanical measurements in the cell. Particularly, unlike individual experimental measurements, the deterministically inferred result approximates an effective ensemble average that is significantly more stable against the biological variability in cell contractility for a given cell shape, reducing variance that may otherwise obscure patterns in data. Finally, evaluated with both traction field and adhesion distribution, the extrapolation by DeepMorphoTM across cell types and substrate materials suggests the learning of common mechanics of cell contractility [Murrell et al. 2015; Oakes et al. 2014; Rape et al. 2011; Tan et al. 2003].

2.4 Results

2.4.1 Substrate displacement and cell traction accurately inferred from a shape sequence of a cell are stable against biological variability in contractility for a given cell shape and high-frequency noise.

A standard time-lapse TFM experiment with fluorescent cell imaging was performed to obtain the bead and cell image sequences (Section 2.6). Substrate displacement and cell traction were respectively calculated from the bead images with a Particle Image Velocimetry (PIV) and a Fourier Transform Traction Cytometry (FTTC) algorithm as described previously [Bauer et al. 2021; Liberzon et al. 2020; Thielicke and Sonntag 2021]. Without the need to address the noise in image segmentation (Fig. 2.8), the cell images were segmented to extract the cell shapes, which were then represented as the Signed Distance Functions (SDFs). SDFs are 2D scalar fields where each value in the field represents the distance to the cell boundary and the geometry is implicitly represented as the zero-level-set. Less affected by the biological variabilities in cell contractility for a given cell shape, DeepMorphoTM deterministically and accurately infers the effective ensemble-average displacement field at a time instance solely from a short sequence of cell shapes through a U-NET style 2D CNN [Ronneberger et al. 2015]; then, a standard TFM

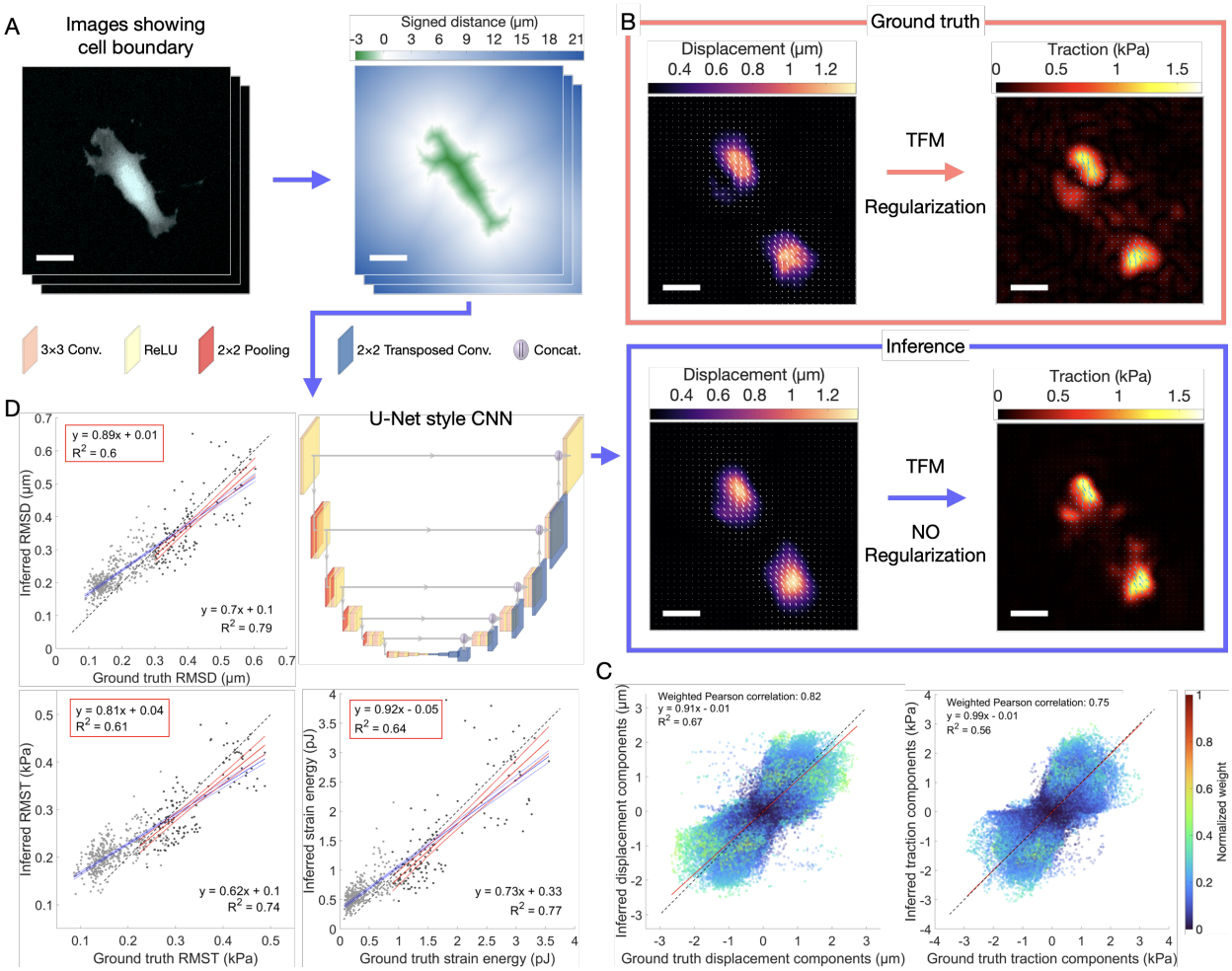

Figure 2.1: A shape sequence of a cell reveals effective ensemble-average cell substrate displacement through DeepMorphoTM, allowing the calculation of contractility. A. Workflow of DeepMorphoTM. First, a short sequence of cell images is transformed to geometries represented as SDFs. The SDFs are then fed into a U-NET style 2D CNN. Finally, the displacement vector field at a time instance is inferred and the traction vector field is calculated from the inferred displacement without the need of regularization. **B.** Example ground truth displacement and traction demonstrate that DeepMorphoTM accurately infers the vector fields. Additionally, the inferred traction contains less background noise than the ground truth. (Scale bar: 30 μm.) **C.** Comparison between inferred and ground truth vector component for displacement and traction indicates accurate inference in effective ensemble, as shown by the linear regression close to $y = x$. The R^2 values are lowered by the conflict between the biological variability in cell contractility for a given cell shape in the ground truth measurement and the stability in the inference from DeepMorphoTM. **D.** Comparison between inferred and ground truth RMSD, RMST, and strain energy demonstrates good alignment between the inferred and ground truth mean displacement, mean traction, and total strain energy per vector field, for cell with RMSD above 0.3 μm (red). Noise in ground truth displacement of 0.1041 μm RMSD (Fig. 2.6B) significantly affected the fitting, as is shown by linear fitting for all data (blue). (553 time instances, n=18.)

algorithm, such as FTTC, without regularization stably computes the traction from the inferred displacement [Butler et al. 2002] (Fig. 2.1A,B).

Notably, the traction is not inferred directly. To directly infer the traction, the neural network needs to be trained on the traction measurement data. Problematically, the computation of the ground truth is unstable, where bounded but high-frequency noise in the displacement measurement can be amplified into unbounded perturbation that spreads throughout the ground truth traction. As confirmed by an L-curve test, the ground truth measurement forms an L-shaped curve that indicates instability (Fig. 2.6A). Usually, regularization is applied to address this instability, but even with significant effort, the recovered traction is not the exact true traction [Brask et al. 2015; Huang et al. 2019; Schwarz et al. 2002; Suñe-Auñón et al. 2017]. Regularization relies on the information about the data which is often not known definitively but rather assumed. The deviation of the assumption from the truth not only hinders the noise from being removed correctly, but also introduces bias to the computed traction. Furthermore, due to the lack of standard procedure on regularization, the bias or error is inconsistent across studies, with biased training data leading to inaccurate models and quantification.

To circumvent those issues, DeepMorphoTM does not directly infer the traction but displacement. The displacement measurement usually does not contain significant artificial bias or unbounded noise and thus makes good training data. More importantly, the computation of the traction from the inferred displacement is stable. The stability arises

from the limited presence of high-frequency noise in inferred displacement, as verified by an L-curve test where the inferred displacement produces a roughly horizontal curve (Fig. 2.6A). In other words, while experimentally collected displacement data contains high-frequency noise that destabilizes the TFM computation and heavily contaminates the traction, the low-noise inferred displacement mitigates the need for regularization and avoids the accompanied problems, offering stability, consistency, and accuracy through DeepMorphoTM.

In the CNN, the contracting encoder gradually extracts spatiotemporal features at different levels from the input SDF sequence. The expanding decoder hierarchically reconstructs the displacement field from the features and recovers the resolution of the output. The skip connections directly pass the features at different levels from the encoder to decoder to enhance the spatial precision of the displacement distribution. Highly compressed scalar latent features are learned at the bottleneck to promote the learning of global properties, such as the total momentum and energy of a cell. To counter the variance in the data, an ensemble of five models were trained and combined by averaging the output. To train each model, the original dataset was augmented by randomly rotating or flipping each sample. The training was done by minimizing the mean over losses between each inferred and ground truth displacement vector component, following L1 loss function:

$$L = |U_i - \hat{U}_i|$$

where U_i and $\hat{U}_i$ denotes ground truth and inferred displacement vector component. Respectively, 903, 111, and 553 partially-overlapping cell sequences from 16, 6, and 18 different cells were used for training, validation, and testing.

DeepMorphoTM demonstrates great accuracy on spatial and global quantities, as well as stability against the biological variability in cell contractility for a given cell shape. To prevent the background vectors from diluting the evaluation of meaningful displacement and traction, a strain-energy-derived weight was applied on each vector in the evaluations. Because strain energy

$$U = \frac{1}{2} V \sigma \epsilon = \frac{1}{2} \frac{V}{E} \epsilon^2 = \frac{1}{2} \frac{V}{E} \sigma^2$$

where V is volume; E is substrate Young's modulus; σ is stress; ϵ is strain, the weight for each vector was formulated to be the square of the greater norm between the ground truth and inferred vectors, normalized by the sum of the weights per vector field:

$$w_i = \frac{\max(n_i, \hat{n}_i)^2}{\sum_{i=1}^{n} \max(n_i, \hat{n}_i)^2}$$

where n_i and $\hat{n}_i$ are the norm of a ground truth and inferred vector respectively. Accounting for spatial distribution, the comparison between the ground truth and inferred vector components revealed a linear relation of approximately $y = x$, reflecting the high accuracy of the inferred vector fields (Fig. 2.1C). Our deterministic model, by design, does not incorporate the variance in the displacement and traction within and among cells of

the same shape, so that the inference may be less affected by the biological variability, possibly creating the spread of the data (Fig. 2.1C). Apart from the spatial distribution, the average displacement and traction per vector field and strain energy were also evaluated. The field averages were quantified by Root Mean Squared Displacement (RMSD) and Root Mean Squared Traction (RMST). The noise level was quantified in RMSD to be 0.1041 µm from the displacement measured from separately acquired bead image pairs of the same cell-free stationary substrate areas (Fig. 2.6B). Despite the perturbation by noise by up to approximately 35%, linear regression on inference vs. ground truth for cells with RMSD over 0.3 µm yielded a fitted line close to $y = x$ for RMSD, RMST, and strain energy, indicating the accurate inference of the field averages and strain energy (Fig. 2.1D). Like in the spatial distribution, the variance in the field averages suggests potential biological variability in contractility for a given cell shape, that is not modelled by our approach. Furthermore, DeepMorphoTM demonstrated excellent temporal consistency through the course of cell locomotion (Supplemental Video).

2.4.2 Variation in the experimental measurements of square patterned cells displays biological variability in contractility for a given cell shape.

Even under carefully controlled experimental conditions, such as culture media and temperature, cells with the same shape exhibit nonidentical, although similar, substrate

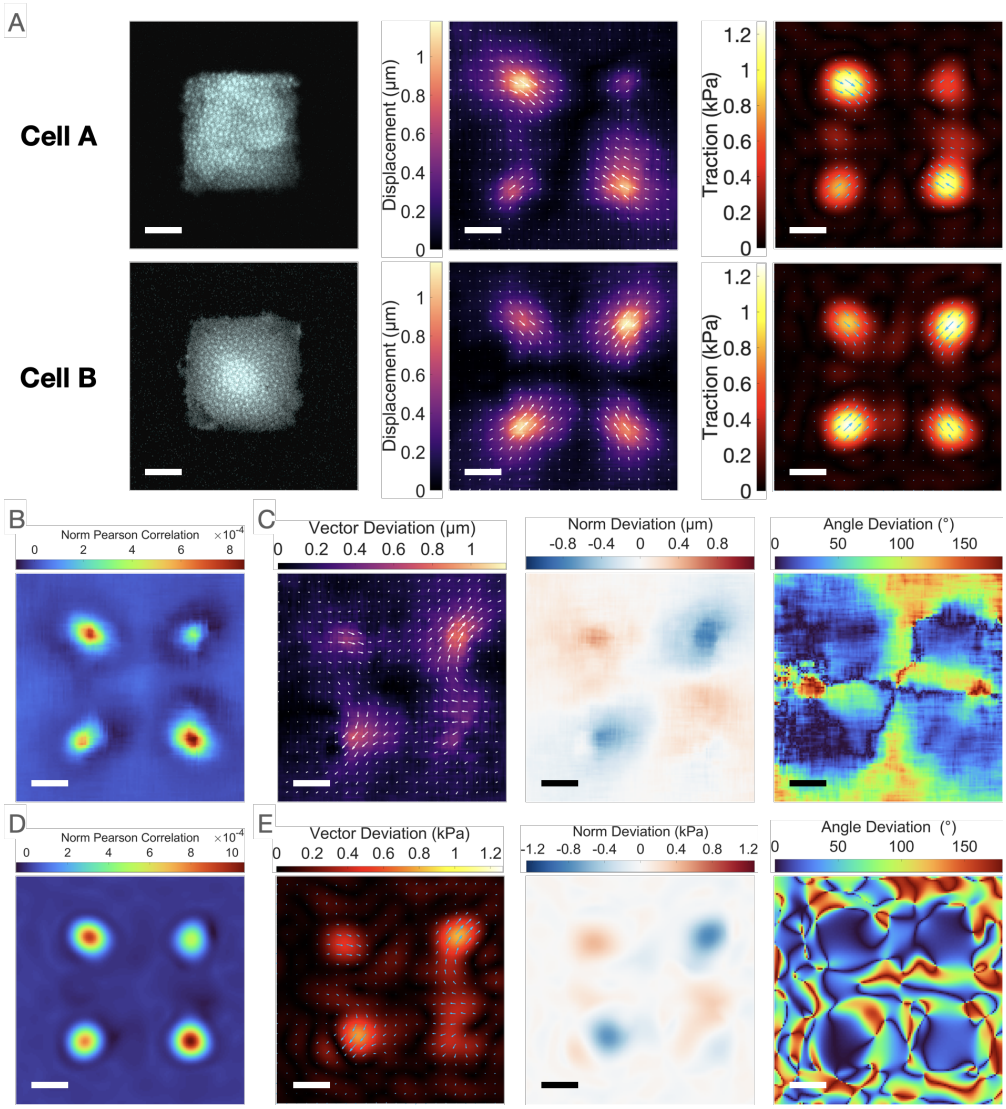

Figure 2.2: Biological variability is prominent in the contractility of square patterned cells. A. Two cells confined on square shaped adhesive protein patterns have nearly identical shapes but generate evidently different substrate displacement and traction. **B.** and **D.** The norm Pearson correlation map shows the similarity in the displacement and traction norm fields respectively between the two patterned cells. High correlation colocalized with large displacement and traction. **C.** and **E.** Vector difference, norm deviation, and angle deviation map show the variation between respectively the displacement and traction created by two patterned cells. The variation comes from the magnitude rather than the direction. (Scale bar: 15 μm.)

displacement and traction [Bastounis et al. 2011; Ghabache et al. 2021; Inagaki and Katsuno 2017]. Like other heterogeneous and stochastic behaviors of the cell, this biological variability in cell contractility for a given cell shape may obscure experimental measurements, necessitating replications to uncover the trend behind widely dispersed data. To be robust against the biological variability, DeepMorphoTM takes a deterministic approach that distills the effective ensemble-average contractility from the experimental measurements, reducing variance in the collected data and potentially the need for experimental replications. With this design, however, the inferred result is not identical to the ground truth which contains the biological variability. Therefore, the quantification of the biological variability is required to estimate the contribution of this variability in the discrepancy between individual inference and ground truth. The closer the variability to the discrepancy, the more accurate DeepMorphoTM possibly is in inferring the effective ensemble average. As an initial examination of the biological variability, experimentally measured displacement and traction from square adhesively patterned cells with nearly identical shapes were respectively compared to each other (Fig. 2.2A). The norm Pearson correlation map illustrates structural similarity in the vector norm fields between two patterned cells (Fig. 2.2B,D). Expectedly, high correlation between cells colocalizes with large displacement and traction. Vector difference, norm deviation, and angle deviation map uncover the variation between respectively the displacement and traction created by two patterned cells (Fig. 2.2C,E). At high displacement and traction area, while the angle

deviation is negligibly small, the vector difference and norm deviation are nontrivial and similar in magnitude, suggesting the biological variability to be primarily in stress distribution but not mechanical balance.

2.4.3 The discrepancy between inference and ground truth potentially arises from biological variability in contractility for a given cell shape, with the temporal information in cell shape altering the inference.

While DeepMorphoTM is accurate in effective ensemble, the discrepancy between individual ground truth and inference exists. The discrepancy is expected to be primarily contributed by the biological variably in contractility for a given cell shape. To quantify this biological variability for patterned cells and discrepancy for nonpatterned cells, four different metrics were employed: the weighted Norm Pearson Correlation (wNPC), the weighted Vector Deviation (wVD), the weighted Absolute Norm Deviation (wAND), and the weighted Angle Deviation (wAD). wNPC measures the linear correlation between the norm of two vector fields and reveals the similarity in the structure or relative distribution of the norm of the vectors. The value scales from -1 to 1, where 1 indicates identical structure; 0 indicates no similarity; -1 indicates inversely related structure. wVD is the vector distance between two vector fields, contributed by the difference in the magnitude

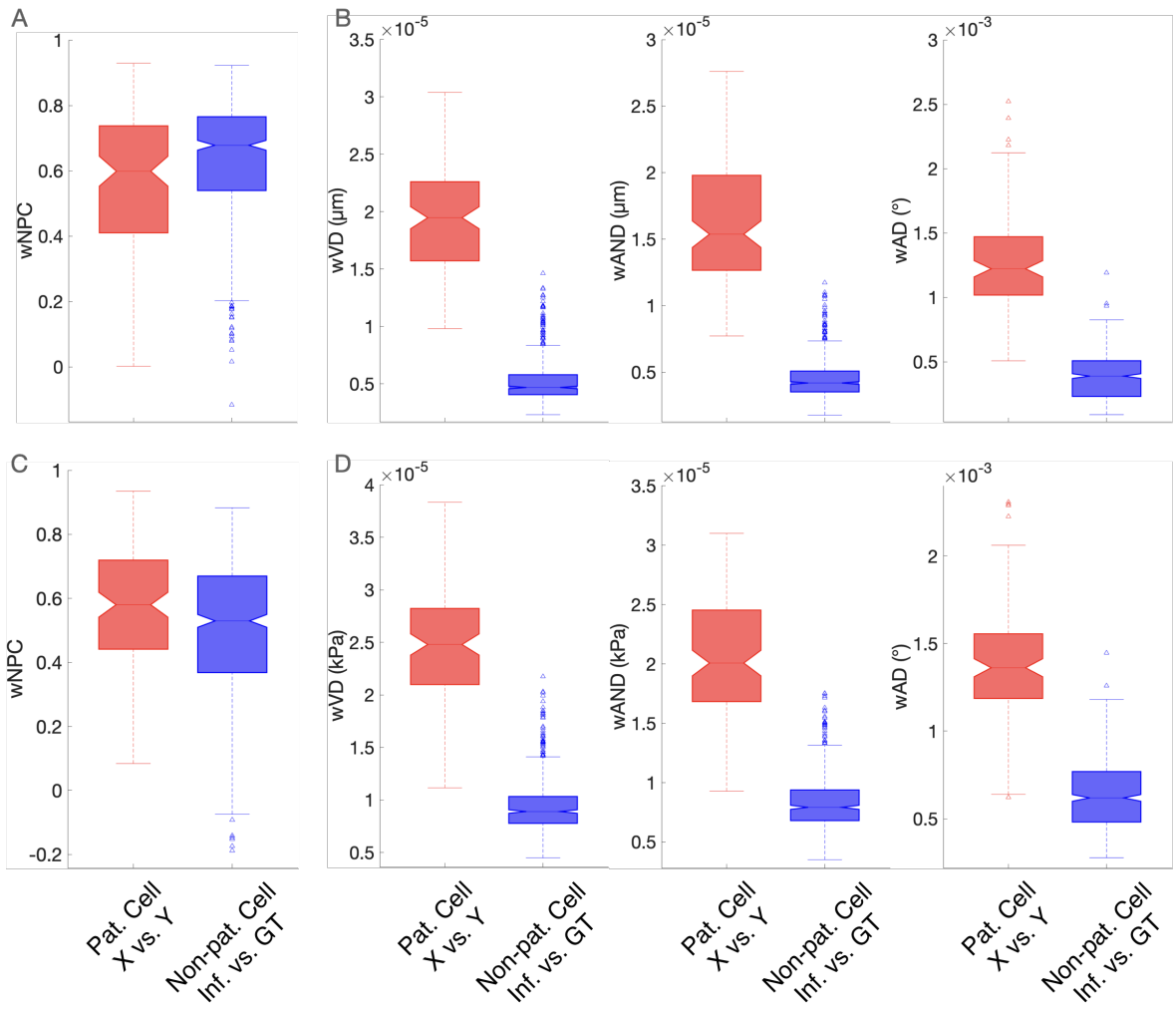

Figure 2.3: The inference and ground truth differ approximately by the extent of the biological variability for a given cell shape. wNPC (**A**, **C**), wVD, wAND, and wAD (**B**, **D**) among displacement (**A**, **B**) and traction (**C**, **D**) respectively of patterned cells (red) and those between nonpatterned inferred and ground truth (blue). Each box displays the median as the central mark, while the lower and upper edges represent the 25^{th} and 75^{th} percentiles, respectively. The whiskers extend to the most extreme nonoutlier data. Outliers are individually plotted using $\triangle$ marker. The metrics on patterned cells quantify the biological variability in cells with a square shape and are considered the baseline to the evaluation of nonpatterned ground truth and inference. The inference by DeepMorphoTM is designed to be stable against biological variability and hence deviates from the ground truth by at least the extent of the biological variability on average. Therefore, by meeting the baseline, the evaluation indicated DeepMorphoTM to be accurate in effective ensemble. (Pat. Cell: 126 data pairs, n=7. Non-pat. Cell: 553 time instances, n=18.)

and direction. wAND shows the absolute deviation in magnitude between two vector fields. wAD denotes the difference in the direction between two vector fields and scales from 0° to 180°.

To generate the biological variability baseline for the evaluation between the ground truth and inference, the displacement and traction of patterned cells were first augmented by rotation and flipping, and then compared, with the four metrics, respectively between each two cells. The evaluation then followed the same metrics, with the outcome bordering the biological variability baseline (Fig. 2.3). Particularly, wAD is negligibly small for both the baseline and evaluation. This result suggests that DeepMorphoTM inference may differ from experimental measurements predominately by the extent of the biological variability for a given cell shape; other source of the deviation, including the error in the inference and background noise in the ground truth measurement, may be small. Notably, for both the patterned cells in the baseline and nonpatterned cells in the evaluation, some comparison yielded low and even negative wNPC. These outliers may be attributed to the biological variability that is apparent in square-patterned cells, wherein cells may have metastable states of contractility across multiple independent contractile axes, allowing weakly correlated distributions of traction at load-bearing adhesions (Fig. 2.7). The prominence of this effect in the patterned cells might also cause the baseline to be higher in wVD and wAND. wVD and wAND were also affected by the moduli of the substrates, where the baseline was 20 kPa and the evaluation 25 kPa. Moreover, DeepMorphoTM is also stable

against noise in segmentation, while the accuracy of segmentation alters the geometry and the inference (Fig. 2.8).

Interestingly, altering temporal information in the input during training or inference implies the nontrivial role of the temporal evolution of cell geometry in cell contractility. At inference, feeding the input sequence in reverse to a model trained on forward sequences results in lower accuracy, suggesting irreversible cell deformation due to contractility (Fig. 2.9). Moreover, models trained on greater input time span and time resolution yield higher accuracy particularly in wNPC and wAD (Fig. 2.10). These outcomes suggest that the evolution of cell geometry reflects the dynamical process of contractility that exists beyond the time instance at which the contraction happens [Sigaut et al. 2021].

Although the inferred displacement does not contain significant high-frequency noise to trigger the ill-posedness, the ground truth and baseline displacement does, necessitating regularization. In this work, the noise was assumed to be separable from the true displacement in the frequency domain, rationalizing the usage of the ideal lowpass filtering on the ground truth displacement data. To reduce computational cost, although possibly different for each displacement data, the optimal frequency threshold per sample was assumed to not vary substantially in each dataset; therefore, a single threshold was determined by the L-curve test and applied to an entire dataset (Fig. 2.6A). Further, to demonstrate the influence of the assumption on the frequency profile of the displacement data, the same evaluation was repeated with the traction computed with a wide range of

regularization thresholds (Fig. 2.11).

2.4.4 Extrapolation by DeepMorphoTM across cell types and substrate materials implies common mechanics of cell contractility.

DeepMorphoTM models the mechanical relationship between cell shape and contractility. The underlying mechanics of cell contractility is expected to be similar across cell types and substrate materials [Murrell et al. 2015; Oakes et al. 2014; Rape et al. 2011; Tan et al. 2003]. If so, the methodology and even inference of DeepMorphoTM should be generalizable. Specifically, while the magnitude of the inferred vectors varies, the relative spatial distribution is expected to be consistent to some degree. To confirm this generalizability, the traction of PC3/PC3-AR cells in different media testosterone concentrations on 12 kPa PDMS substrates and CHO-K1 cells on glass substrates were inferred with DeepMorphoTM trained on 3T3 cells on 25 kPa substrate. As expected, the spatial distribution and orientation of the inferred traction is consistent with the experimentally measured measurement for PC3/PC3-AR cells (Fig. 2.4A,B). Regardless of the cell types, because DeepMorphoTM was trained on a stiffer substrate of 25 kPa, the inferred displacement is lower than the measured displacement in a 12 kPa substrate by a ratio of 12 kPa / 25 kPa (Fig. 2.4C). If the inferred displacement is naïvely scaled by 25 kPa / 12 kPa, the magnitudes of the inferred and measured traction also match

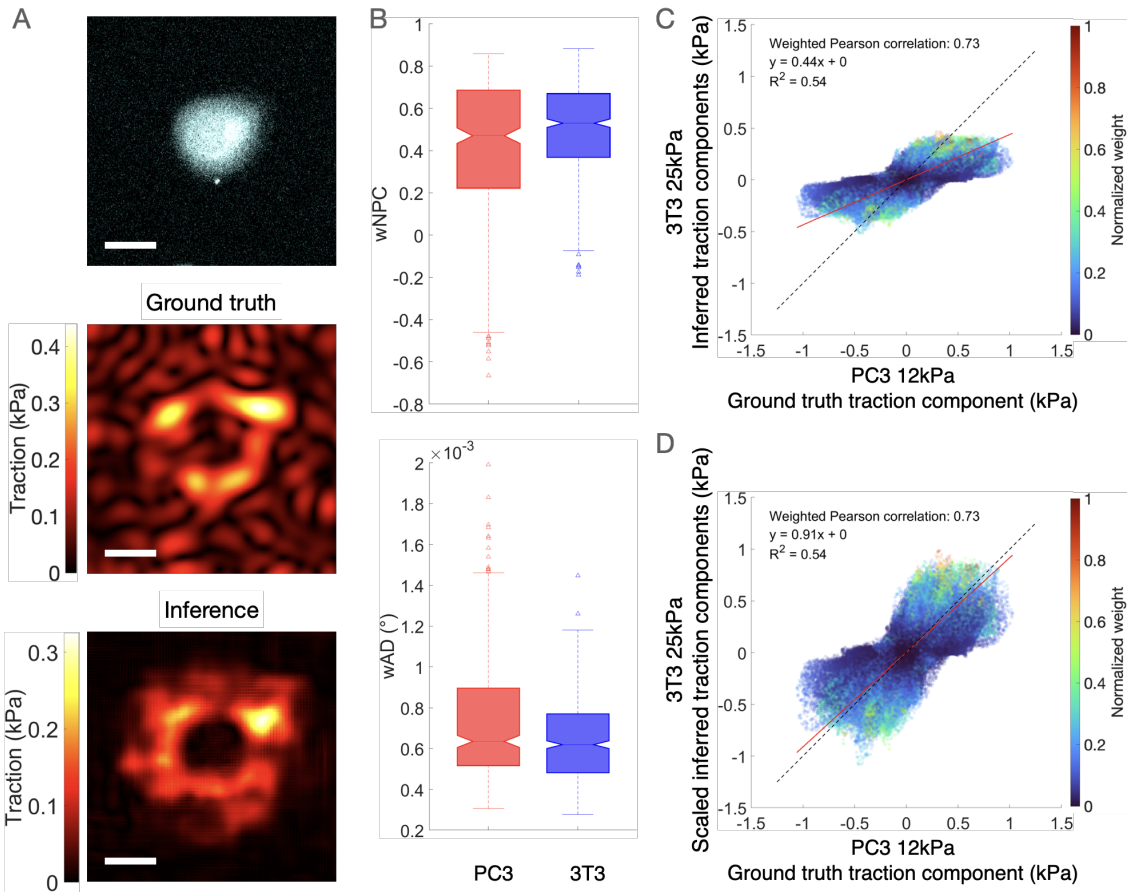

Figure 2.4: DeepMorphoTM trained on 3T3 cells on 25 kPa PDMS extrapolates traction for cells of untrained types, treatments, and substrate modulus. A. A PC3 cell under 1nM testosterone on 12 kPa PDMS with the corresponding ground truth traction and the traction inferred by the model trained on 3T3 cells on 25 kPa PDMS. While the magnitude of the ground truth and inference is different, the spatial distribution matches well. As a typical case, noise in the ground truth can be difficult to suppress. (Scale bar: 25 µm.) **B.** wNPC and wAD of the PC3/PC3-AR extrapolation test (red) and 3T3 in-distribution evaluation (blue). The extrapolation yields similar performance as interpolation. **C.** Inferred vs. PC3/PC3-AR 12kPa traction vector component. The inference is consistently lower in magnitude as reflected by the slope of the linear fitting. The weighted Pearson correlation and R2 are similar to that of the in-distribution evaluation dataset (Fig. 2.1C). **D.** Scaled inferred vs. PC3/PC3-AR 12kPa traction vector component. Scaling the inferred displacement by a constant factor of 2.08 to compensate for the difference in substrate stiffness between 12 and 25 kPa results in the scaled inferred traction and a fitting of approximately $y = x$. (396 time instances, n=27.)

(Fig. 2.4D). The inferred traction was also overlaid with adhesions of CHO-K1 cells, revealing that while the adhesions did not fully colocalize with the traction, the traction colocalized with the adhesions (Fig. 2.5, 2.12). As expected, traction cannot exist beyond the adhesions yet not all adhesions are load-bearing. Additionally, the resolution of the inferred traction did not match that of the adhesions, due to the lower resolution of the ground truth measurement used in training and thus of the inference as well. To ensure comparable resolution, the adhesions were Gaussian blurred by a series of extent (Fig. 2.12A). Pearson correlation between the norm of the traction and the adhesions were calculated (Fig. 2.12B). The correlation was weighted by the square of the inferred traction, so that the comparison highlighted adhesions that were inferred to be load-bearing (Fig. 2.12C).

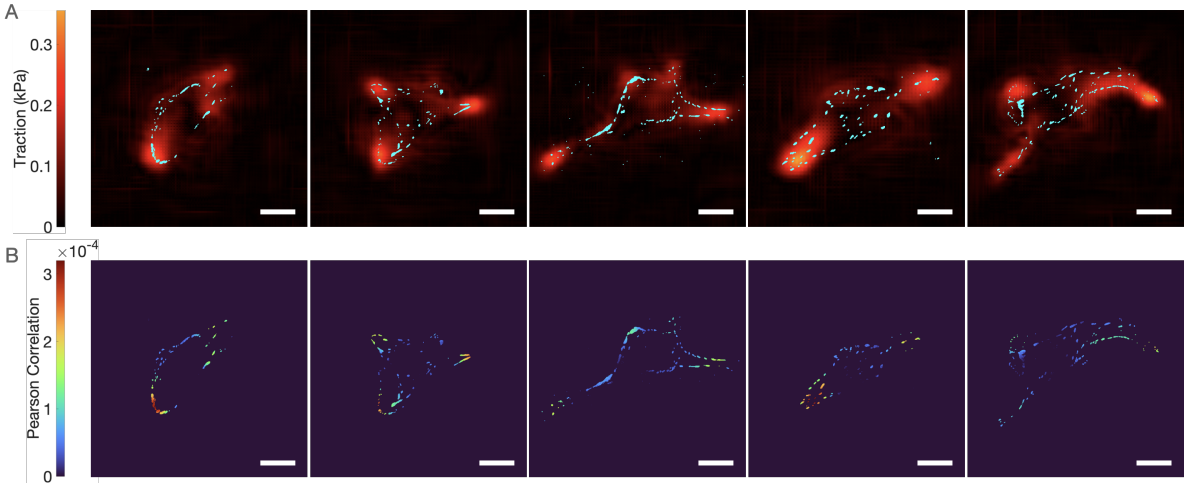

Figure 2.5: Traction inferred by DeepMorphoTM trained on 3T3 cells colocalizes with the adhesions of cells of an untrained type. A. Inferred traction and segmented adhesions overlays suggest correlation between traction and adhesions across cell types. **B.** Pearson correlation maps between the inferred traction and segmented adhesions highlight that traction colocalizes with adhesions at cell extrusions. (Scale bar: 20 µm.)

2.5 Discussion

In this study, substrate displacement and cell traction are accurately inferred solely from a cell shape sequence with the DL method DeepMorphoTM. Biological variability under controlled experimental settings injects variance to data and impedes the discovery of the meaningful patterns. The deterministic approach models an effective ensemble average of the experimentally measured data, significantly weakening the biological variance in quantification. However, this design also introduces discrepancy between the inference and ground truth. This added discrepancy does not indicate error in the inference, but rather suggests the stability of DeepMorphoTM against the biological variability in contractility for a given cell shape. As such, our method accurately infers the effective ensemble-average vector fields and global quantities. Further, without high-frequency noise in the inferred displacement, the need for regularization in the computation of traction, which challenges traditional TFM algorithms, was negated. Finally, the extrapolation by DeepMorphoTM across cell types and substrate materials matches the experimentally measured traction fields and adhesion distribution, implying the modelling of common mechanics of cell contractility.

The common approach taken by traditional TFM algorithms through the Green's function or finite element analysis faces an ill-posed inverse problem [Huang et al. 2019; Schwarz et al. 2002; Suñe-Auñón et al. 2017]. The displacement is a Fredholm integral of the first kind of the traction. The computation of the traction exploits the inverse relation

involving effectively the displacement gradient. From a mechanical perspective, displacement itself is not directly related to traction, but through displacement gradient, which is associated with strain and then stress. Therefore, the magnitude of the calculated traction depends on the spatial frequency of the displacement, but not on the magnitude of the displacement. In this way, however small in magnitude, noise in the displacement with high spatial frequency translates to large error in the traction. To compound the issue, the slowly decaying Green's function propagates every local noise to the entire traction field, rendering the computation highly unstable. As the common resort, regularization has been employed to address the instability. However, regularization itself presents challenges. Accurate prior knowledge about the displacement and traction needs to be known in advance, and then appropriate regularization strategy should be employed accordingly. Specifically, because each regularization method addresses a specific type or part of noise, to perfectly regularize the computation of traction: all the assumptions about the displacement and traction must be correct; the noise must be separable from the true data based on these assumptions; all types of noise are addressed by the regularization methods. Guaranteeing all these requirements is by no means trivial if possible at all. Furthermore, each computation requires a one-off effort to address the above challenges, creating an additional challenge of high computation cost and low applicability, especially for large dataset required by DL. For this reason, a single frequency threshold was applied to the entire dataset to calculate the ground truth traction. Additionally, due to the lack of closed

form solution, many regularization methods adopt optimization-based algorithms that also have high computational complexity [Huang et al. 2019; Suñe-Auñón et al. 2017]. Avoiding the ill-posedness and all the challenges coming with it, DeepMorphoTM utilized solely cell shape to infer the displacement rather than traction. The reliability and accuracy of the training data is hereby not limited by the quality of the computation of the measured traction. Although the inverse problem is faced again in the computation of the traction from the inferred displacement, the ill-posedness and instability are resolved by the inferred displacement, as proven by the L-curve test (Fig. 2.6A).

Under a carefully controlled setting, biological variability injects variance or fluctuation to and obscure patterns in the data, including the relationship between cell shape and the mechanical profile of the cell. This variability may be heterogeneous and/or stochastic and live among or within individual cells. However, were the variability in contractility given a cell shape to be accounted for, the heterogeneity may be modelled deterministically with additional input information; otherwise, generative or probabilistic approaches may be used to address both heterogeneity and stochasticity. Possible sources of the variability include the fluctuation of the traction, the spatiotemporally heterogeneous mechanical properties of the cell material due to discrete cytoskeletal structures, and the reduction of 3D volume to 2D shape in measurement. Firstly, while inertia effects are negligibly small in the cell system, thereby making it highly overdamped, underdamped wave-like fluctuations of the traction have been observed, suggesting active biological processes to generate such

fluctuations [Bastounis et al. 2011; Ghabache et al. 2021; Inagaki and Katsuno 2017]. Secondly, the interior mechanical properties of cells, such as local modulus and viscosity, may vary among cells and over time, altering the relationship between the shape and forces. Thirdly, while the cell is a 3D mechanical system, our current method only utilized 2D shape information, which could simply be incomplete. Employing input of 3D cell geometry could remove the variability from this source with additional experimental and computational cost. Accordingly, free from additional experimental effort, generative or probabilistic approaches may be preferred for utility.

Despite the biological variability in the training data, DeepMorphoTM accurately distills the relationship between cell shape and traction. This relationship follows the laws of physics, and thus cell shape is fundamentally driven by mechanics. For instance, the lower accuracy from feeding the input sequence in reverse during inference fits the expectation that the deformation and locomotion of cells are an irreversible process with viscous energy dissipation (Fig. 2.9); however, the different yet similar accuracy for models taking input of different time span and time resolution hints at the quasi-static nature of biological processes (Fig. 2.10). Regardless of cell type or substrate material, cells with a certain shape are expected to exhibit similar spatial distributions of traction including the direction, because of the common mechanism of contractility and mechanical balance [Murrell et al. 2015; Oakes et al. 2014; Rape et al. 2011; Tan et al. 2003]. Indeed, the inferred traction matched the experimental measurement simply after scaling the inferred

displacement and colocalized with the adhesions of cells of untrained types on untrained substrates. Further, this common fundamental mechanical relationship also suggested great generalizability and potential of DeepMorphoTM that this DL approach could easily be trained and applied to different cell types and substrate materials. We believe that DeepMorphoTM offers researchers who do not have access to TFM a novel and extremely simplified approach to incorporate contractility measurement into their studies. Even beyond current studies, valuable insights can be easily gained from historical cell image data through retrospective mechanical analysis with our method.

2.6 Materials and Methods

2.6.1 Synthesis of Compliant Silicone Substrates for TFM

To perform TFM experiments, polydimethylsiloxane (PDMS) substrates of 12 kPa, 20 kPa, and 25 kPa were prepared as described previously [Ghagre et al. 2021; Yoshie et al. 2018, 2019]. In brief, PDMS solutions were supplied by mixing same weight ratio of component A and B of commercial PDMS (NuSil® 8100, NuSil Silicone Technologies, Carpinteria, CA) with respectively 0.36%, 0.45%, and 0.48 % w/w of Sylgard 184 PDMS crosslinking agent (Dimethyl, methyl hydrogen siloxane, which contains methyl terminated silicon hydride units) to obtain substrates with a modulus of 12 kPa, 20 kPa, and 25 kPa. Then, 170 µl of each solution was applied to the clean 22×22 mm glass coverslips and cured at 100 °C for

two hours. For traction force microscopy, prepared PDMS substrates were coated with 1 µm thick layer of fiduciary particles using spin coater (Laurell Technologies, WS-650 Spin Processor) and incubated at 100 °C for an hour.

In order to covalently bind fibronectin to PDMS substrates, Sulfo-SANPAH (ThermoFisher Scientific) solution dissolved in 100 mM HEPES was added on top of the substrates and they were exposed to UV for 2 minutes. After UV activation, Sulfo-SANPAH solutions were removed and 5 µg/ml fibronectin (Sigma) solution diluted in PBS was added on top of the samples, followed by incubation in room temperature for 9-12 hours. Finally, fibronectin solutions were removed, and substrates were rinsed with PBS three times. After UV sterilization of coated substrates, trypsinized cells were seeded on top of the samples and they were allowed to adhere overnight.

2.6.2 UV based Micropatterning of proteins on Silicone Substrates

To measure biological variability, we adhesively micropatterned silicone substrates with square shapes using a UV-patterning system (PRIMO, Alveole Lab, Paris, France). PDMS substrates were incubated with poly-L-lysine (PLL; Sigma) solution (5 mg/mL) prepared in 0.1 M HEPES buffer (pH 8.5) for 1 h at room temperature, followed by rinsing with Milli-Q water. Positively charged PLL electrostatically adsorbs onto the negatively charged surface of silicone substrates and allows protein attachment after printing. The substrates

were then incubated with polyethylene glycol succinimidyl valeric acid (PEG-SVA; Laysan Bio) prepared in 0.1 M HEPES buffer (pH 8.5) for 30 min at room temperature, followed by thorough rinsing with phosphate buffered saline (PBS), pH 7. PEG-SVA acts as an antifouling brush layer that repels protein attachment. The substrates were then covered with the UV sensitive photoinitiator solution of PLPP (Alveole Lab, Paris, France) and placed on the stage of a microscope (Nikon Ti2 Eclipse) equipped with the UV- patterning system. To generate the patterns, we used the open-source graphics software programs Inkscape and ImageJ to generate binary 8-bit mask image files that were loaded into PRIMO's control software. The desired pattern was generated by a digital micromirror array in the PRIMO system and projected using a 375 nm UV laser with an intensity of 29 mW/mm2 via a 20×/0.45NA objective. The projected pattern results in localized photodegradation of the antifouling PEG-SVA brush, in the shape of the desired pattern. An exposure dose of 20 s was adequate to complete photodegradation of the PEG-SVA brush. Following UV exposure, we washed the substrates with PBS and incubated them for 1 h at room temperature with a mixture of fluorescently labeled bovine serum albumin (BSA; Alexa Fluor 555 conjugate, Thermo Fisher, 5 µg/mL) and fibronectin (40 µg/mL, Sigma) in PBS to adsorb the protein to the exposed PLL surface. Excess protein was rinsed off with PBS prior to cell seeding.

2.6.3 Cell Culture

NIH-3T3 Mus musculus, mouse cell line obtained from ATCC were cultured in Dulbecco's modified Eagle medium (DMEM) (Wisent) supplemented with 10% fetal bovine serum (FBS) (Wisent) and 1% Penicillin-Streptomycin antibiotic (P/S) (Thermo Fisher). The cells were incubated at 37 °C in 5% CO_2 environment and they were allowed to grow on the substrates for 18 hours before imaging. For biological variability experiments, cells were seeded on the patterns for 1 h at 37 °C in 5% CO_2 environment, followed by a gentle wash with PBS to remove nonattached cells to avoid nonspecific attachments. Cells were further incubated for 16 - 18 h (on patterns) before imaging at 37 °C in 5% CO_2 environment.

PC3-AR is an androgen receptor (AR)-positive prostate cancer cell line that was generated by stably expressing mGFP-tagged AR by means of lentiviral transduction (OriGene) of the highly metastatic, AR-negative prostate cancer cell line, PC3, obtained from the American Type Culture Collection (ATCC). PC3-AR has been used in previous studies to investigate the mechanisms of AR in mediating prostate cancer progression and invasiveness [Miao et al. 2017]. Cells were cultured in RPMI-1640 culture media without phenol red (Wisent Inc.), supplemented with 10% fetal bovine serum (Wisent Inc.) and 1% penicillin–streptomycin (P/S, Wisent Inc.); 0.5 ug/mL puromycin was used in culture media to select for cells expressing mGFP-AR. In this study, various androgen concentrations were applied to PC3-AR. PC3-AR cells were plated in androgen-free media supplemented with different concentrations of synthetic testosterone R1881 (Toronto

Research Chemicals Inc.) to reflect low (0.1 nM), normal (1 nM), and high (10 nM) androgen conditions [Chatterjee et al. 2019; Lessard et al. 2012]. Androgen-free media consists of RPMI-1640 media with 10% charcoal-stripped fetal bovine serum (CSS; Gibco, Thermo Fisher Scientific Inc.), 1 % P/S, and 0.5 µg/mL puromycin. The androgen-deprivation condition consisted of only androgen-free media.

Chinese Hamster Ovary-K1 (CHO-K1) cells stably expressing chicken paxillin-WT-EGFP were obtained from the lab of Dr Rick Horowitz (University of Virginia, Charlottesville, VA). CHO-K1 cells were grown in low glucose (1.0 g/L) Dulbecco's modified Eagle's medium (DMEM; Thermo Fisher Scientific, Cat. no. 11,885-084) supplemented with 10% fetal bovine serum (FBS; Thermo Fisher Scientific, Cat. no. 10082-147), 1% non-essential amino acids (Thermo Fisher Scientific, Cat. no. 11140-050), 25 mM 4-(2-hydroxyethyl)-1-piperazineethanesulfonic acid (HEPES; Thermo Fisher Scientific, Cat. no. 15630-080) and 1% penicillin- streptomycin (Thermo Fisher Scientific, Cat. no. 10378-016). Cells were maintained in 0.5 mg/mL Geneticin-418 (G418; Thermo Fisher Scientific, Cat. no. 11811-031) antibiotic selection to maintain paxillin-EGFP expression. ibidi µ-slides (Ibidi, Cat. no. 80826) were coated with freshly made 2 µg/mL solution of fibronectin diluted in phosphate buffered saline (PBS) from a stock of 0.1% human plasma fibronectin (Sigma Aldrich, Cat. no. F-0895) overnight at 4 °C. Slides were then washed 3x with PBS. Cells were lifted with trypsin/EDTA (Thermo Fisher Scientific, Cat. No. 25200-056) and 2000 cells/cm2 were seeded into wells of the

µ-slides (Ibidi, Cat. no. 80826) and left in the incubator overnight. The samples were placed in a Chamlide TC-L-Z003 stage top environmental control incubator (Live Cell Instrument, Seoul, South Korea) at 37 °C with 5% CO_2 while imaging.

2.6.4 Traction Force Microscopy

Active contractile stress in actin cytoskeleton were quantified using TFM as previously described [Koushki et al. 2020; Yoshie et al. 2018, 2019; Butler et al. 2002]. NIH 3T3 cells were cultured on fibronectin coated compliant PDMS substrates of known moduli and a thin PDMS layer of embedded fiduciary fluorescent particles was spin coated on the top surface. After 12 hours incubation at 37 °C, cells were stained with Cell Tracker Green CMFDA dye (Thermo Fisher) as per manufacturers protocol to visualize cell shape. To capture the force image, the stained cells and fluorescent particles were imaged simultaneously using Leica TCS SP8 confocal microscope with low magnification (×10/NA 0.4 air objective) at a resolution of 0.28 µm/pixel. The null force images of the fluorescent particles were acquired at the end of the experiment by detaching the cells from the substrate surface.

For PC3-AR cells, substrate surfaces were functionalized using Sulfo-SANPAH (Sigma-Aldrich, MO, United States) and coated with 5 µg/ml fibronectin to facilitate cell attachment at 4°C overnight, as previously described [Molter et al. 2022; Yoshie et al. 2019]. Prior to cell plating, cells were labelled with CellTracker Orange CMTMR Dye

(Invitrogen; Thermo Fisher Scientific, Inc.), then plated in their respective experimental androgen condition. Cells were then allowed to settle on the PDMS substrate and adjust to their chemical environment for 48 hours before imaging. Immediately before imaging, cell nuclei were labelled with HOESCHT 33342 (1:10000 dilution; Thermo Fisher Scientific, Inc.). For imaging, cells were mounted on a confocal microscope (Leica TCS SP8 with a 40×/0.85 NA objective). During imaging, cells were maintained at 37°C and 5% CO_2 (perfusing 100% humidity prebottled 5% CO_2 in synthetic air). Labelled cells, mGFP-AR, nuclei, and fiduciary TFM bead displacements were simultaneously imaged using fluorescent and transmission microscopy.

The displacement vector field was calculated from the drift-corrected force and null-force fluorescent bead images by PIVlab and OpenPIV [Liberzon et al. 2020; Thielicke and Sonntag 2021]. The traction was computed with FTTC implemented by pyTFM [Bauer et al. 2021]. Regularization implemented an ideal low-pass filtering on the displacement.

Total Internal Reflection Fluorescence Microscopy (TIRF) Microscopy of CHO-K1 Cells

CHO-K1 cells were imaged using a Spectral Diskovery TIRF unit (Spectral Applied Research, Richmond Hill, ON) attached to an inverted Leica DMI6000B microscope (Leica Microsystems, Wetzler, Germany) with a Leica Plan ApoChromat 63x/1.47 NA TIRF oil immersion objective lens. Paxillin-EGFP was imaged with 1% power (10% power, 10x

pulsing) from a 100 mW 488nm diode laser (Spectral Applied Research) with a TIRF depth of 100 nm, an ORCA-Flash4.0 (Hamamatsu, Japan), 5 sec exposure time and 2x2 binning to obtain high signal-to-noise images. Pixel size was 0.1244 µm with a and was equipped with two ImagEMX2 Digital EM-CCD Cameras (Hamamatsu, Hamamatsu City, Japan). Images were captured with an EGFP emission filter (ET 525/50nm) using MetaMorph 7.1 image acquisition software (Molecular Devices Inc.) and custom designed TIRF controls (Quorum Technologies Inc., Guelph, ON).

2.6.5 Training and testing data preparation

Cell images were processed and segmented with CellProfiler with selected modules and methods, including ReduceNoise, Minimum Cross-Entropy, Otsu, and Robust Background [Stirling et al. 2021] . The SDF was computed by BWDIST Distance transform of binary image through MATLAB. The dimension of the SDF and displacement field were rescaled to fit the CNN. The distance value of SDF and vector value of the displacement field were rescaled to the same order of magnitude to assist training convergence. The 2D SDF sequence was stacked to make 3D input.

2.6.6 Construction and training of the CNNs

The deep learning algorithm was implemented through PyTorch [Paszke et al. 2019]. The CNNs were structured similar to U-Net [Ronneberger et al. 2015]. The spatial dimension of

the input and output was 256×256. The time dimension of the input data was processed as channel. Each convolution layer was paired with a following ReLU activation. In the encoding path, convolution blocks consisted of two 3×3 convolutional layers and a following 2×2 max pooling layer. The initial convolution block used 80 channels. Four convolution blocks succeeded, with the first layer of each block doubling the number of channels. Three consecutive 3×3 convolution layers and a 2×2 convolution layer were used to reduce the features to scalars. The first 3×3 convolution layers doubled the number of channels and the 2×2 convolution layer did again. At the beginning of the decoding path, four 2×2 consecutive transposed convolution layers were applied first to recover the dimension of the features from the scalars. Then followed four transposed convolution blocks, each with two 3×3 convolution layers and a 2×2 transposed convolution layer. Each transposed convolution block took as input the upstream output as well as the features from the skip connection. Finally, the number of channels were gradually reduced to two by four 3×3 convolution layers.

Optimization was done with Adam optimizer with an initial learning rate of 0.0001 [Kingma and Ba 2014]. 30 samples were used per batch. Each training session was performed on a single NVIDIA V100 GPU approximately over 7 h 45 min for 240 epochs.

2.7 Acknowledgments

The authors sincerely thank YuChen Huang, Xuemeng Sun, and Weixin Wu for their support with the experiments, and Cameron Hastie for manuscript comments. Funding: AJE acknowledges support from NSERC RGPIN/05843-2014, NSERC EQPEQ/472339-2015, CIHR Grant # 143327, NSERC RGPIN-2020-07169 and NSERC RTI/00348-2018. YT acknowledges support from IVADO MSc Excellence Scholarship; McGill MEUSMA Award. The authors acknowledge support from Compute Canada.

2.8 Supporting material

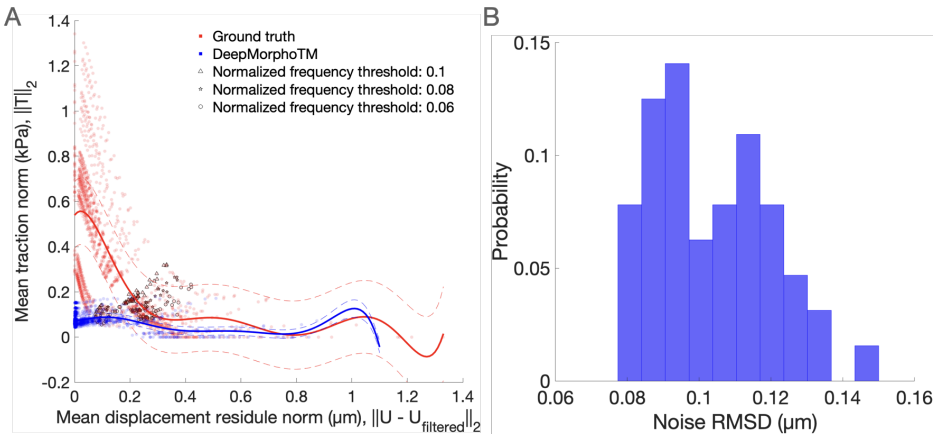

Figure 2.6: Noise in the ground truth measurement is quantified. A. L-curve test for the computation of traction from the ground truth measurement and inferred displacement. The test for the ground truth produced an L-shaped curve, indicating that small high-frequency perturbations in the measured displacement cause significant contamination of the traction. The ground-truth computation is unstable and requires regularization. On the contrary, the computation with the inferred displacement results in an approximately horizontal curve and therefore does not suffer from this issue. (54 time instances, n=18.) **B.** Root Mean Squared Displacement of the measurement on undeformed substrate reveals the noise profile of the displacement measurement. (425 time instances, n=14.)

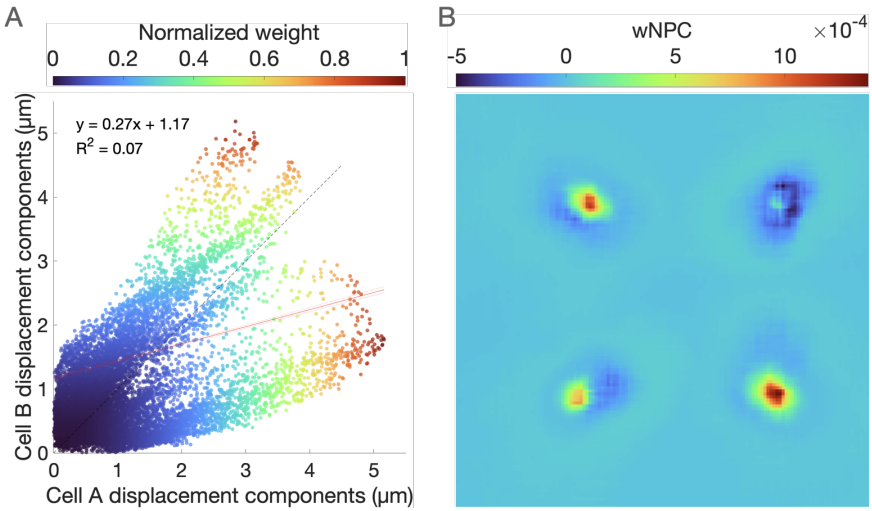

Figure 2.7: Evident in square patterned cells, metastable states of contractility across multiple independent contractile axes may create drastically different distributions of traction at load-bearing adhesions. A. Comparison of the norm of the displacement of the two square patterned cells in Fig. 2.2A exposes low correlation for large displacement. **B.** In addition to the expected large positive correlation, wNPC shows significant negative correlation at high-displacement area.

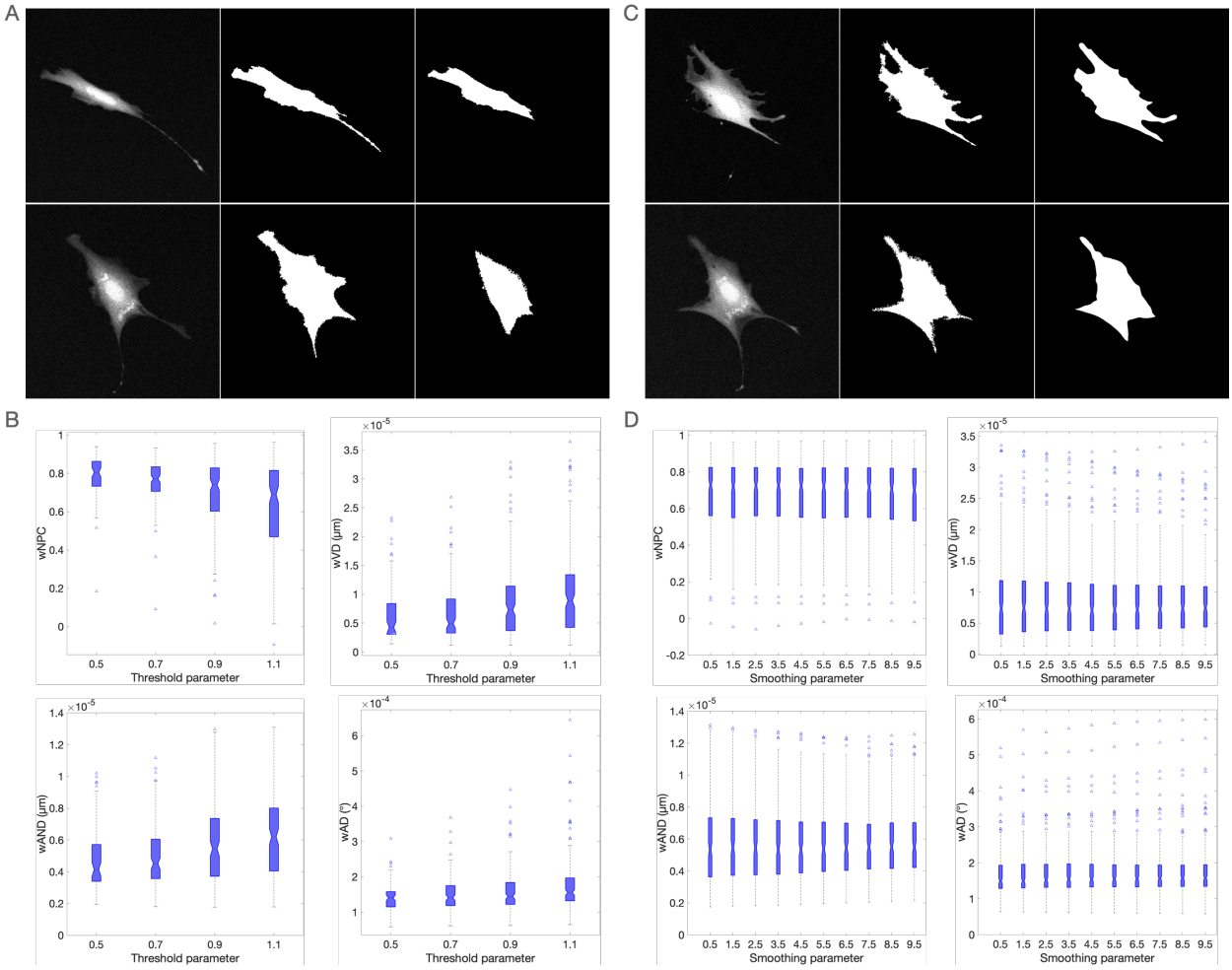

Figure 2.8: The inference is stable against the quality of segmentation, where the accuracy of the geometry has a more substantial influence than the precision. A. Example cells and the corresponding segmentations under threshold parameters of 0.5 and 1.1 are different in structure and thus accuracy. **B.** Input generated with different thresholds result in nontrivial difference in wNPC, wVD, wAND, and wAD between the ground truth and inferred displacement. The effect of threshold depended on the threshold applied in the generation of the training data. In this work, a lenient threshold was employed to deliver accurate segmentation. Threshold parameters lower than 0.5 predominantly generated clearly wrong segmentations. **C.** Example cells and the corresponding segmentations under smoothing parameters of 0.5 and 9.5 are different in boundary smoothness, while the change in structure and accuracy is marginal. **D.** Input generated with different smoothing result in trivial difference in wNPC, wVD, wAND, and wAD between the ground truth and inferred displacement. (205 time instances, n=6.)

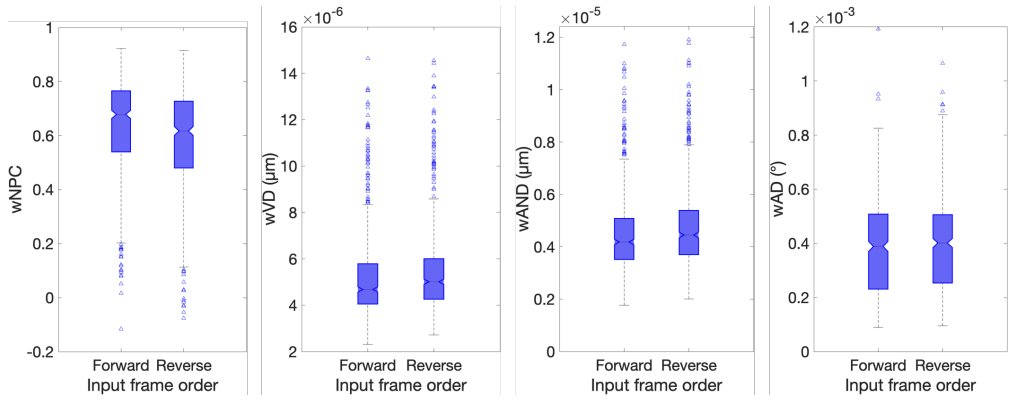

Figure 2.9: Lower inference accuracy from the input in reversed sequence suggests irreversible cell deformation due to contractility. (553 time instances, n=18)

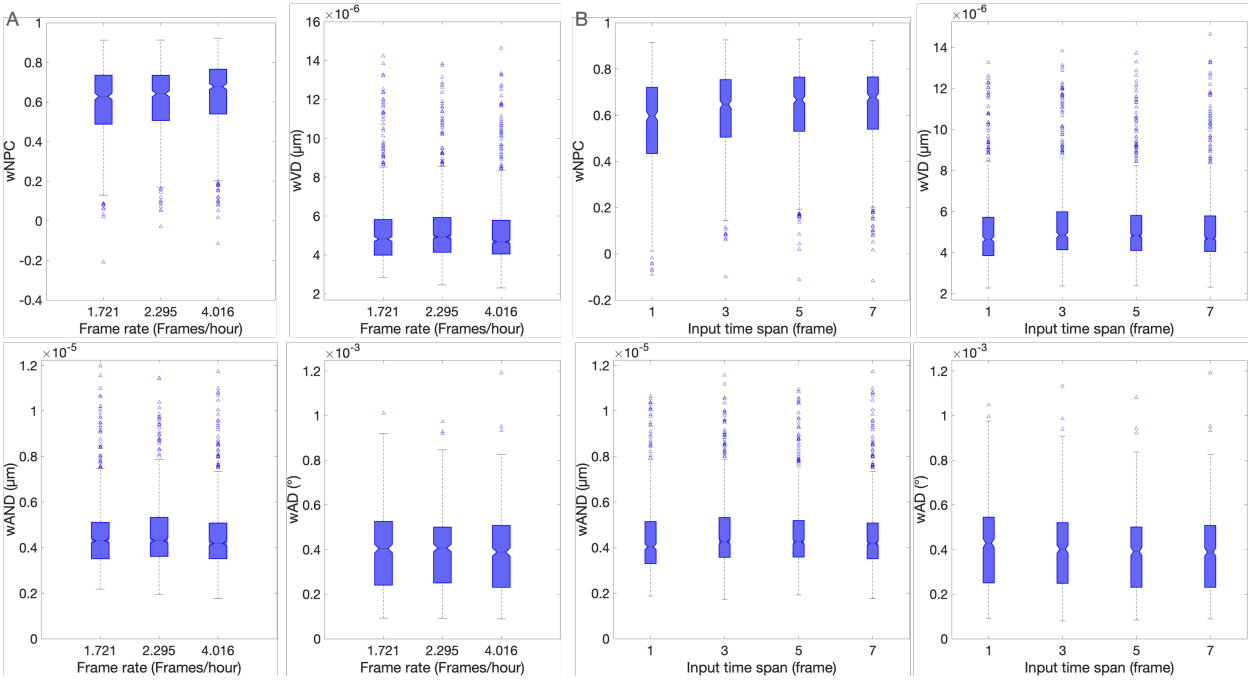

Figure 2.10: Training with greater input time span and time resolution enables higher inference accuracy. The effect is more prominent in wNPC and wAD than in wVD and wAND. (553 time instances, n=18.)

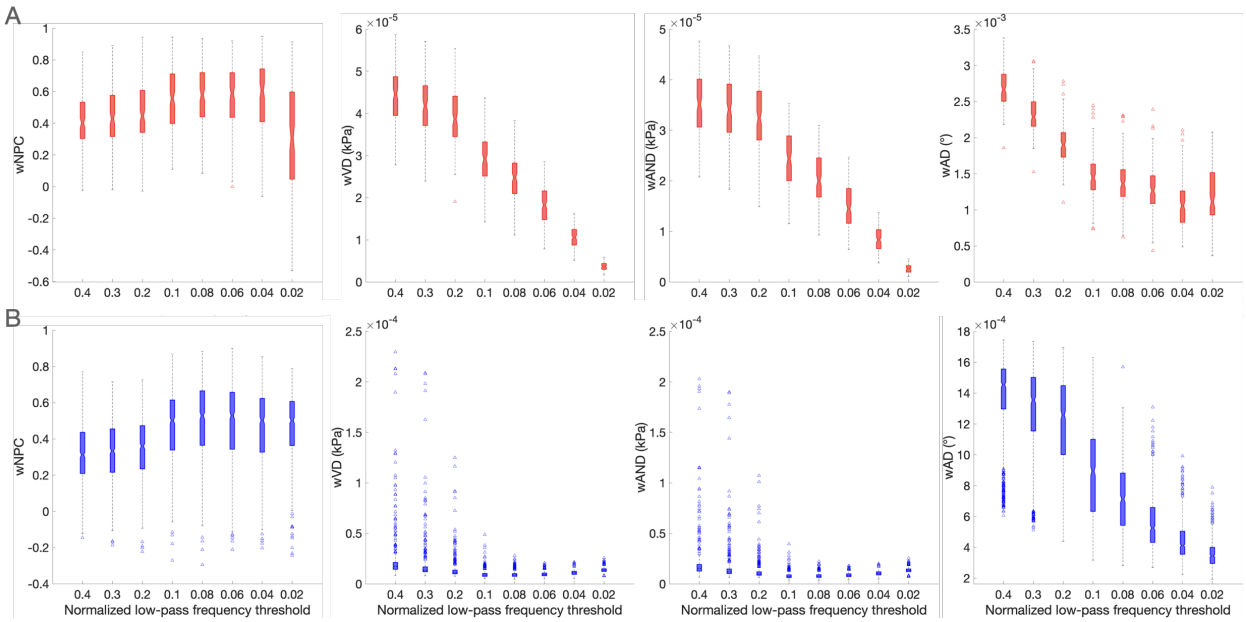

Figure 2.11: The extent of regularization affects the evaluations. As the cutoff frequency of the low-pass filter lowers, information in the displacement is removed progressively from high to low frequency. **A.** For biological variability baseline with patterned cells, when more higher frequency information is removed from two displacement fields, the displacement and therefore traction fields become more similar until the retained information is extremely small. **B.** For the evaluation between ground truth and inference, when more high frequency information is removed from the ground truth displacement, the similarity between displacement and thus between traction fields rises initially and then decreases. Initially, noise is removed from the ground truth, reducing the difference between the ground truth and inference. Then, further regularization erodes meaningful information in the ground truth, causing the ground truth to deviate from the inference. Particularly, wAD monotonously decreases in the examined threshold range because the direction of the vectors is a low-frequency feature. (Pat. Cell: 126 data pairs, n=7. Non-pat. Cell: 553 time instances, n=18.)

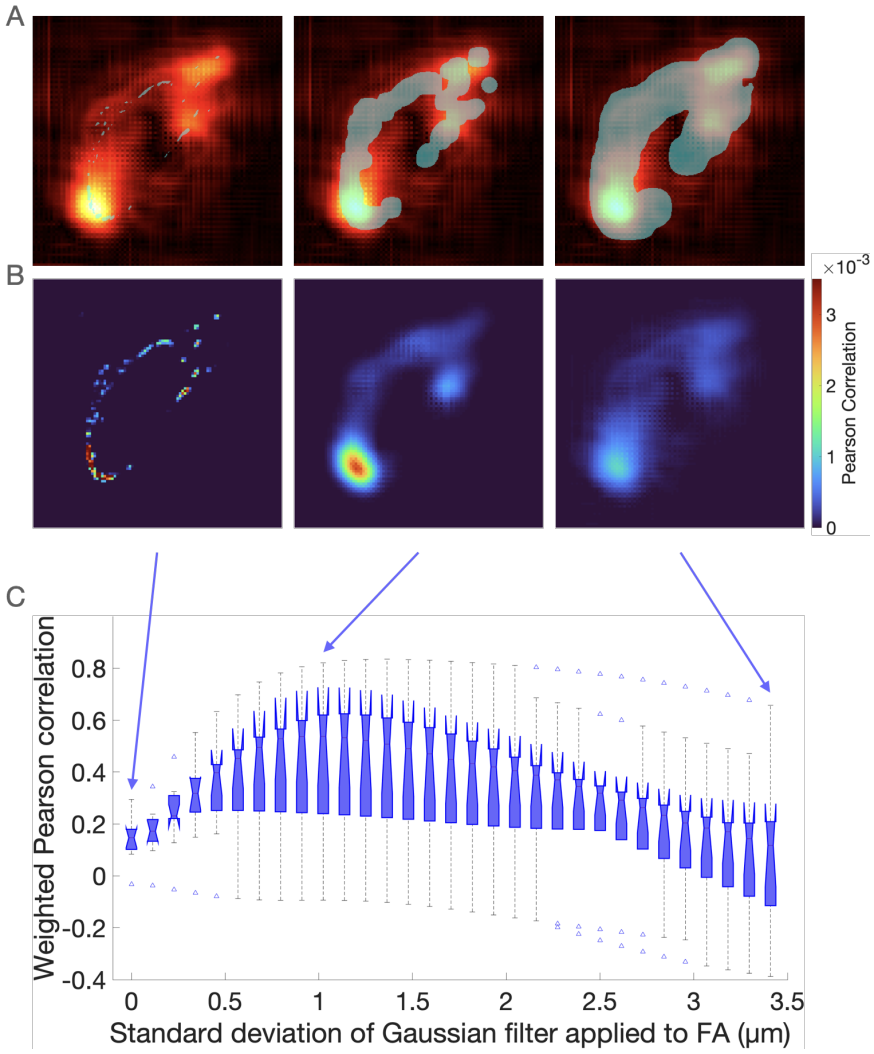

Figure 2.12: Lower resolution of the inferred traction creates discrepancy in spatial frequency between the traction map and adhesions. **A.** Segmented adhesions of a cell were Gaussian-dilated by standard deviation of 0, 1.1365, and 3.4095 µm, from left to right, and overlaid on the inferred traction. Due to the lower resolution of the training data, traction of resolution lower than that of adhesions was inferred. The dilation compensates for the discrepancy in resolution. **B.** Corresponding to **A.**, the Pearson correlation maps between the inferred traction and Gaussian-filtered segmented adhesions quantifies the colocalization of adhesions and traction. **C.** Weighted Pearson correlation between inferred traction fields and Gaussian-filtered adhesions for different cells uncovered the resolution of the inferred traction. The peak correlation indicted a spatial standard deviation in the traction of approximately 1.1 µm from the adhesions. The weight emphasized the correlation between meaningful traction and the colocalized adhesions, neglecting the possibly non-load-bearing adhesions beyond the area of meaningful traction. (n=10.)

References

Nathalie Q Balaban, Ulrich S Schwarz, Daniel Riveline, Polina Goichberg, Guy Tzur, Izhak Sabanay, Dan Mahalu, Samuel Safran, Alexander Bershadsky, and Lia Addadi. Force and focal adhesion assembly. *Nature Cell Biology*, 3(5):466–472, 2001.

Omar A Banda, Chandran R Sabanayagam, and Joseph H Slater. Reference-free traction force microscopy platform fabricated via two-photon laser scanning lithography enables facile measurement of cell-generated forces. *ACS Applied Materials & Interfaces*, 11(19): 18233–18241, 2019.

Effie Bastounis, Ruedi Meili, Baldomero Alonso-Latorre, Juan C del Álamo, Juan C Lasheras, and Richard A Firtel. The scar/wave complex is necessary for proper regulation of traction stresses during amoeboid motility. *Molecular Biology of the Cell*, 22:3995–4003, 2011.

Andreas Bauer, Magdalena Prechová, Lena Fischer, Ingo Thievessen, Martin Gregor, and

Ben Fabry. pytfm: A tool for traction force and monolayer stress microscopy. *PLOS Computational Biology*, 17:e1008364, 2021.

Martin Bergert, Armin Erzberger, Ravi A Desai, Irene M Aspalter, Andrew C Oates, Guillaume Charras, and Guillaume Salbreux. Confocal reference free traction force microscopy. *Nature Communications*, 7:12814, 2016.

Jonatan Bohr Brask, Guillem Singla-Buxarrais, Marina Uroz, Romaric Vincent, and Xavier Trepat. Compressed sensing traction force microscopy. *Acta biomaterialia*, 26:286–294, 2015.

James P Butler, Iva M Tolić-Nørrelykke, Ben Fabry, and Jeffrey J Fredberg. Traction fields, moments, and strain energy that cells exert on their surroundings. *American Journal of Physiology-Cell Physiology*, 282(3):C595–C605, 2002.

Payel Chatterjee, Michael T Schweizer, Jared M Lucas, Ilsa Coleman, Michael D Nyquist, Sander B Frank, Robin Tharakan, Elahe Mostaghel, Jun Luo, Colin C Pritchard, et al. Supraphysiological androgens suppress prostate cancer growth through androgen receptor–mediated dna damage. *The Journal of clinical investigation*, 129(10):4245–4260, 2019.

Micah Dembo and Yu-li Wang. Stresses at the cell-to-substrate interface during locomotion of fibroblasts. *Biophysical Journal*, 76:2307–2316, 1999.

Micah Dembo, Tracy Oliver, Akira Ishihara, and Kenneth Jacobson. Imaging the traction

stresses exerted by locomoting cells with the elastic substratum method. *Biophysical Journal*, 70:2008–2022, 1996.

X. Duan and J. Huang. Deep-learning-based 3d cellular force reconstruction directly from volumetric images. *Biophysical Journal*, 121:2180–2192, 2022.

Adam J Engler, Shamik Sen, H Lee Sweeney, and Dennis E Discher. Matrix elasticity directs stem cell lineage specification. *Cell*, 126:677–689, 2006.

Jianping Fu, Yu-li Wang, Mengsu Yang, Ravi A. Desai, and Xiaojun Yu. Mechanical regulation of cell function with geometrically modulated elastomeric substrates. *Nat. Methods*, 7:733–6, 2010.

Elisabeth Ghabache, Yuansheng Cao, Yuchuan Miao, Alex Groisman, Peter N Devreotes, and Wouter-Jan Rappel. Coupling traction force patterns and actomyosin wave dynamics reveals mechanics of cell motion. *Molecular Systems Biology*, 17, 2021.

Atul Ghagre, Ankur Chaturvedi, Balkees AlRasheed, Stefanos Mourdikoudis, and Abhijit Ghosh. Pattern-based contractility screening, a reference-free alternative to traction force microscopy methodology. *ACS Applied Materials & Interfaces*, 13(17):19726–19735, 2021.

Sina Ghassemi, Giovanni Meacci, Shu Liu, Alexander Gondarenko, Abhinav Mathur, Pere Roca-Cusachs, and Michael P. Sheetz. Cells test substrate rigidity by local contractions on submicrometer pillars. *Proc. Natl. Acad. Sci. U. S. A.*, 109:5328–33, 2012.

Sung Sik Hur, Yuejin Zhao, Yin-Sheng Li, Elliot Botvinick, and Shu Chien. Live cells exert 3-dimensional traction forces on their substrata. *Cellular and Molecular Bioengineering*, 2(4):425–436, 2009.

N. Inagaki and H. Katsuno. Actin waves: Origin of cell polarization and migration? *Trends in Cell Biology*, 27:515–526, 2017.

Donald E Ingber. Mechanobiology and diseases of mechanotransduction. *Annals of Medicine*, 35:564–577, 2003.

Diana E Jaalouk and Jan Lammerding. Mechanotransduction gone awry. *Nature Reviews Molecular Cell Biology*, 10:63–73, 2009.

Diederik P. Kingma and Jimmy Ba. Adam: A method for stochastic optimization. *arXiv preprint arXiv:1412.6980*, 2014.

Newsha Koushki, Ajinkya Ghagre, Luv Kishore Srivastava, Chris Sitaras, Haruka Yoshie, Clayton Molter, and Allen J Ehrlicher. Lamin a redistribution mediated by nuclear deformation determines dynamic localization of yap. *bioRxiv*, page 2020.03.19.998708, 2020. doi: 10.1101/2020.03.19.998708.

Benoit Ladoux and René-Marc Mégé. Mechanobiology of collective cell behaviours. 2017. doi: 10.1038/nrm.2017.98.

Y. LeCun, B. Boser, J. Denker, D. Henderson, R. Howard, W. Hubbard, and L. Jackel.

Handwritten digit recognition with a back-propagation network. In *Advances in Neural Information Processing Systems*, volume 2, 1989.

Jennifer Lee, Mia Leonard, Tracy Oliver, Akira Ishihara, and Kenneth Jacobson. Traction forces generated by locomoting keratocytes. *Journal of Cell Biology*, 127:1957–1964, 1994.

Wesley R Legant, Jordan S Miller, Brandon L Blakely, and Adam R Cohen. Measurement of mechanical tractions exerted by cells in three-dimensional matrices. *Nature Methods*, 7 (12):969–971, 2010.

Laurent Lessard, David P Labbé, Genevieve Deblois, Louis R Bégin, Serge Hardy, Anne-Marie Mes-Masson, Fred Saad, Lloyd C Trotman, Vincent Giguere, and Michel L Tremblay. Ptp1b is an androgen receptor–regulated phosphatase that promotes the progression of prostate cancerar-induced ptp1b expression in prostate cancer. *Cancer research*, 72(6):1529–1537, 2012.

Alex Liberzon, Davide Lasagna, Mathias Aubert, Pete Bachant, Theo Käufer, jakirkham, Andreas Bauer, Boyko Vodenicharski, Cameron Dallas, Joe Borg, tomerast, and ranleu. Openpiv/openpiv-python: Openpiv - python (v0.22.2) with a new extended search piv grid option (0.22.2), 2020.

Sarah A Maskarinec, Christian Franck, David A Tirrell, and Guruswami Ravichandran. Quantifying cellular traction forces in three dimensions. *Proceedings of the National Academy of Sciences*, 106(53):22108–22113, 2009.

Lu Miao, Lin Yang, Rui Li, Daniel N Rodrigues, Mateus Crespo, Jer-Tsong Hsieh, Wayne D Tilley, Johann De Bono, Luke A Selth, and Ganesh V Raj. Disrupting androgen receptor signaling induces snail-mediated epithelial–mesenchymal plasticity in prostate cancerenzalutamide promotes prostate cancer emp. *Cancer research*, 77(11):3101–3112, 2017.

Clayton W Molter, Eliana F Muszynski, Yuanyuan Tao, Tanisha Trivedi, Anna Clouvel, and Allen J Ehrlicher. Prostate cancer cells of increasing metastatic potential exhibit diverse contractile forces, cell stiffness, and motility in a microenvironment stiffness-dependent manner. *Frontiers in Cell and Developmental Biology*, 10:932510, 2022.

Michael Murrell, Patrick W. Oakes, Martin Lenz, and Margaret L. Gardel. Forcing cells into shape: the mechanics of actomyosin contractility. *Nat. Rev. Mol. Cell Biol.*, 16:486–498, 2015.

Patrick W. Oakes, Shiladitya Banerjee, M. Cristina Marchetti, and Margaret L. Gardel. Geometry regulates traction stresses in adherent cells. *Biophys. J.*, 107:825–833, 2014.

Chan Young Park, Dhananjay Tambe, Bohao Chen, Tera Lavoie, Maria Dowell, Anton Simeonov, and Min Shen. High-throughput screening for modulators of cellular contractile force. *Integrative Biology*, 7(11):1318–1324, 2015.

Adam Paszke, Sam Gross, Francisco Massa, Adam Lerer, James Bradbury, Gregory Chanan, Trevor Killeen, Zeming Lin, Natalia Gimelshein, Luca Antiga, et al. Pytorch: An

imperative style, high-performance deep learning library. *Advances in neural information processing systems*, 32, 2019.

Nicoletta I Petridou, Zoltán Spiró, and Carl-Philipp Heisenberg. Multiscale force sensing in development. *Nature Cell Biology*, 19:581–588, 2017.

Sergey V. Plotnikov, Ana M. Pasapera, Benedikt Sabass, and Clare M. Waterman. Force fluctuations within focal adhesions mediate ecm-rigidity sensing to guide directed cell migration. *Cell*, 151:1513–1527, 2012.

Andrew D. Rape, Wei-hui Guo, and Yu-li Wang. The regulation of traction force in relation to cell shape and focal adhesions. *Biomaterials*, 32:2043–2051, 2011.

Ramin Rokhzan, Chandra C Ghosh, Niccole Schaible, Jacob Notbohm, Haruka Yoshie, Allen J Ehrlicher, Sarah J Higgins, Ruyuan Zhang, Hermann Haller, Corey C Hardin, et al. Multiplexed, high-throughput measurements of cell contraction and endothelial barrier function. *Laboratory Investigation*, 99(1):138–145, 2019.

O. Ronneberger, P. Fischer, and T. Brox. U-net: Convolutional networks for biomedical image segmentation. In *Medical Image Computing and Computer-Assisted Intervention*, pages 234–241. Springer, 2015.

Lucas Sigaut, Martina Bianchi, Catalina von Bilderling, and Lia Isabel Pietrasanta.

Correlation of cellular traction forces and dissociation kinetics of adhesive protein zyxin revealed by multi-parametric live cell microscopy. *PLoS One*, 16(6):e0251411, 2021.

David R Stirling, Madison J Swain-Bowden, Alice M Lucas, Anne E Carpenter, Beth A Cimini, and Allen Goodman. Cellprofiler 4: improvements in speed, utility and usability. *BMC Bioinformatics*, 22(1):433, 2021.

W. Thielicke and R. Sonntag. Particle image velocimetry for matlab: Accuracy and enhanced algorithms in pivlab. *Journal of Open Research Software*, 9(1), 2021.

Jennet Toyjanova, Kevin G Cornwell, Benjamin Oswald, Jonathan S Reichner, and Christian Franck. High resolution, large deformation 3d traction force microscopy. *PloS One*, 9(3): e90976, 2014.

Sigrid Van Helvert, Cornelis Storm, and Peter Friedl. Mechanoreciprocity in cell migration. *Nature Cell Biology*, 20:8–20, 2018.

Kyle H Vining and David J Mooney. Mechanical forces direct stem cell behaviour in development and regeneration. *Nature Reviews Molecular Cell Biology*, 18:728–742, 2017.

Y. Wang and Y.-C. Lin. Traction force microscopy by deep learning. *Biophysical Journal*, 120:3079–3090, 2021.

Matthew Wheelwright, Zaw Win, Jennifer L Mikkila, Kamilah Y Amen, Patrick W Alford,

and Joseph M Metzger. Investigation of human ipsc-derived cardiac myocyte functional maturation by single cell traction force microscopy. *PLoS One*, 13(4):e0194909, 2018.

Haruka Yoshie, Newsha Koushki, Rosa Kaviani, Mohammad Tabatabaei, Kavitha Rajendran, Quynh Dang, Amjad Husain, Sean Yao, Chuck Li, John K Sullivan, et al. Traction force screening enabled by compliant pdms elastomers. *Biophysical Journal*, 114 (10):2194–2199, 2018.

Haruka Yoshie, Newsha Koushki, Clayton Molter, Peter M Siegel, Ramaswamy Krishnan, and Allen J Ehrlicher. High throughput traction force microscopy using pdms reveals dose-dependent effects of transforming growth factor-β on the epithelial-to-mesenchymal transition. *Journal of Visualized Experiments*, (143), 2019. doi: 10.3791/59364.

Chapter 3

Discussion

The development of DeepMorphoTM relied on a comprehensive understanding of the mathematics, mechanics, biology, and algorithms that underlie TFM and cell contractility. Introduction (Chapter 1) and manuscript (Chapter 2) have addressed certain facets. This chapter continues to discuss these topics and their impact on the design of DL methodologies.

3.1 The ill-posed inverse problem

3.1.1 Hadamard's well-posedness conditions

Jacques Hadamard established a set of three conditions that define a well-posed problem: (i) the existence of a solution, (ii) the uniqueness of a solution, and (iii) the continuous

dependence of a solution on data [Hadamard 1902; Hansen 2010]. Particularly, the continuous dependence states that any small perturbation, such as noise, in the data must lead to an also small perturbation in the solution. Failing any of the conditions makes a problem "ill-posed". Generally, the inverse of the Fredholm integral equation of the first kind may not have a solution, a unique solution, or a solution that continuously depend on the data, rendering the problem ill-posed based on all three conditions [Delves and Mohamed 1988; Hadamard 2003; Hansen 2010; Kress et al. 1989; Ursell 1974].

With the common substrate properties and boundary conditions, TFM satisfies the existence and uniqueness conditions, violating only the continuous dependence condition. For the inverse problem to have a solution, the Green's function must have a singularity, where a singularity is a point at which the function is not defined [Hansen 2010; Ursell 1974]. In the case of Eq. (1.5), $\mathbf{G}_{in-plane}(\mathbf{r})$ has a singularity at $\mathbf{r} = \mathbf{0}$, and therefore satisfies the existence condition. Furthermore, for the solution to be unique, the mapping from $\mathbf{T}$ to $\mathbf{u}$ by Green's function must be invertible [Hansen 2010]. As $\mathbf{G}_{in-plane}(\mathbf{r})$ is invertible, an inverse of $\mathbf{G}_{in-plane}(\mathbf{r})$ that maps $\mathbf{u}$ to $\mathbf{T}$ exists [Butler et al. 2002; Huang et al. 2009; Schwarz and Soiné 2015]. Therefore, $\mathbf{G}_{in-plane}(\mathbf{r})$ also satisfies the unique solution condition.

The continuous dependence condition is violated when low-magnitude noise in the displacement can be transformed to significant perturbations in the traction field in a manner that depends on the spatial frequency of the noise. The greater the frequency, the

more noise is amplified. The noise strongly contaminate the computed traction and impair the reliability of TFM [Hansen 2010; Mesgarani and Azari 2019]. While various numerical methods have been employed to solve the inverse problem, including Bayesian likelihood, BEM, SVD, FT, and FEA, the violation of the continuous dependence condition has been avoided by none [Butler et al. 2002; Dembo and Wang 1999; Hur et al. 2009, 2012; Schwarz et al. 2002]. The violation of the continuous dependence condition is the very nature of the relationship between traction and displacement.

3.1.2 The slowly decaying Green's function

The relationship between displacement and traction is fundamentally influenced by the property that $\mathbf{G}(\mathbf{r})$ is long-ranged: compared to the point-like traction which decays rapidly in space, $\mathbf{G}_{\text{in-plane}}$ in Eq. (1.5) decays slowly by a factor of $\frac{1}{r}$. In the forward computation of Eq. (1.4), $\mathbf{G}$ is applied to each $\mathbf{T}(\mathbf{r}')$ vector, making each vector produce an influence decaying by $\frac{1}{r}$ over the range of $\mathbf{G}$ in displacement. In this sense, the Green's function functions like a Gaussian filter, casting a smoothing or blurring effect, as each traction vector is "spread out" by the Green's function. At every $\mathbf{r}$, the integration combines $\mathbf{G}(\mathbf{r}-\mathbf{r}')\mathbf{T}(\mathbf{r}')$ "spread out" from all $\mathbf{T}(\mathbf{r}')$. These operations result in the damping of higher-frequency components in the traction field in the forward computation.

The field of traction and of displacement can be described as the sums of sinusoidal waves

of different amplitudes and frequencies in different directions:

$$\begin{aligned} \mathbf{u} &= \textstyle\sum_f \mathbf{u}_f \\ \mathbf{T} &= \textstyle\sum_f \mathbf{T}_f \end{aligned} \tag{3.1}$$

where $\mathbf{u}_f$ and $\mathbf{T}_f$ are the wave components of the displacement and traction. Eq. (1.4) can be rewritten accordingly as:

$$\sum_f \mathbf{u}_f(\mathbf{r}) = (\mathbf{G} * \sum_f \mathbf{T}_f)(\mathbf{r}) = \sum_f (\mathbf{G} * \mathbf{T}_f)(\mathbf{r}) = \sum_f \int_{-\infty}^{\infty} \mathbf{G}(\mathbf{r}-\mathbf{r}')\mathbf{T}_f(\mathbf{r}')\, d\mathbf{r}' \tag{3.2}$$

The damping effect is more pronounced in higher-frequency than lower-frequency traction components. For $\mathbf{T}_f$ with a low frequency thus long period compared to the range of $\mathbf{G}$, information is similar within the effective range of $\mathbf{G}$, so mixing $\mathbf{G}(\mathbf{r}-\mathbf{r}')\mathbf{T}_f(\mathbf{r}')$ would not change the information from each traction vector substantially. However, high-frequency $\mathbf{T}_f$ contains significantly different information in the effective range of $\mathbf{G}$. Different spatial information becomes mixed in space, leading to effective loss of the information. To be more specific, positive and negative amplitudes partially cancel each other and sum up to approximately zero. Thus, the damping is strong for high-frequency components in traction. In other words, the forward computation has a damping or smoothing effect in the mapping from $\mathbf{T}$ to $\mathbf{u}$, where higher-frequency components in traction are damped more significantly, causing the displacement to be smoother than the traction [Hansen 2010].

The inverse computation exhibits the opposite effect: higher-frequency components in displacement are amplified during the computation of traction. This effect can be explained in the forward and inverse view. In the forward view, because $\mathbf{G}(\mathbf{r})$ decays by $\frac{1}{r}$, $\mathbf{T}(\mathbf{r}')$ closer to $\mathbf{r}$ has greater influence over $\mathbf{u}(\mathbf{r})$. If the spatial variation in $\mathbf{T}(\mathbf{r}')$ in the effective range of $\mathbf{G}$ is large enough, information from $\mathbf{T}(\mathbf{r}')$ at $\mathbf{r}'$ close or equal to $\mathbf{r}$ dominates $\mathbf{u}(\mathbf{r})$. In other words, information from high-frequency traction components can be distinguishable in displacement only if the amplitude is exceptionally high. Therefore, higher-frequency components in displacement, although small in amplitude, result in exceptionally large high-frequency traction in the inverse computation.

From the inverse view, the reason is two-folded. First, because every displacement vector contains combined information from the entire traction field through $\mathbf{G}$, $\mathbf{u}(\mathbf{r})$ at each $\mathbf{r}$ propagates information to $\mathbf{T}(\mathbf{r}')$ at all $\mathbf{r}'$ through $\mathbf{G}$. This property exhibits an amplification effect in the sense that local information in the displacement has non-local impacts in traction. The second part of the reason lies in the integro-differential relationship between displacement and traction.

3.1.3 The integro-differential relation

The integro-differential relationship is analogous to that of an integral and its respective derivative. For an integral equation, there is an equivalent differential equation [Ursell 1974]. Because the integration of traction yields displacement, displacement needs to be

differentiated to compute traction. From a mechanical perspective, displacement itself does not have a direct relationship with traction, but through displacement gradient, which is related to strain and then stress. Therefore, the integration in the forward problem essentially becomes differentiation in the inverse problem.

For a given amplitude, the derivative of $\mathbf{u}_f$ linearly increases with the frequency and therefore the magnitude of $\mathbf{T}$ does not depend on the magnitude of $\mathbf{u}_f$ but the frequency. However small in magnitude $\mathbf{u}_f$ is, $\mathbf{u}_f$ can be computed into an arbitrarily large magnitude of $\mathbf{T}$, depending on the frequency. The higher the frequency is, the more $\mathbf{u}_f$ is amplified. Nonetheless, this effect of differentiation is local and does not alone affects the computed traction to the extend in TFM.

Compounded with the first part of the reason from the inverse view, the amplification of higher-frequency displacement component becomes non-local in traction through the Green's function and significantly impact the computed traction. The range of $\mathbf{G}$ determines how far the local derivative of $\mathbf{u}$ is spatially propagated in $\mathbf{T}$. With a long-ranged Green's function, the inverse computation strongly amplifies higher-frequency components in the mapping from displacement to traction.

3.1.4 Noise in the displacement

In practice, noise in the displacement data can come from many sources, including elastic inhomogeneities in the substrate, weak coupling between marker beads and polymer

matrix, deficiencies in the optical setup, and inaccuracy in the tracking routines [Sabass et al. 2008]. While the displacement decays smoothly by a factor of $\frac{1}{r}$, the noise has much higher frequencies. Consequently, the noise is greatly amplified and can strongly corrupts the computed traction [Sabass et al. 2008; Schwarz and Soiné 2015; Schwarz et al. 2002].

3.2 Regularization

3.2.1 The common approach

Lacking the "simpler" smooth pattern of the true displacement, high-frequency noise can be mitigated by regularization, if a distinct assumption(s) about the displacement, i.e., smoothness, or about the traction, i.e., sparsity and smoothness, is known [Delves and Mohamed 1988; Donoho 2006; Hadamard 2003; Hansen 2010; Kress et al. 1989; Mesgarani and Azari 2019; Ursell 1974]. Because solving Eq. (1.4) as is yields noisy traction, a "simplified" solution with suppressed noise is attempted through regularization that encourages a "simpler" or "more regular" solution distinct from the "complex" or "irregular" noise. Often, this attempt is accomplished through introducing additional regularization terms or penalties to the problem. The penalties fulfill the assumptions that are used to additionally constrain and regularize the solution. In this way, regularization may turn the inverse problem of Eq. (1.4) to an optimization problem which finds $\mathbf{T}$ that minimizes an expression formulated by rearranging Eq. (1.4) and adding one or multiple

penalties:

$$\underset{\mathbf{T}}{\operatorname{argmin}} \left[\|\mathbf{G} * \mathbf{T} - \mathbf{u}\|_{p_1}^{q_1} + \sum_{n=1} \lambda_n \|\mathbf{R}_n(\mathbf{T})\|_{p_2}^{q_2} \right] \tag{3.3}$$

where $\underset{\mathbf{T}}{\operatorname{argmin}} [\cdot]$ denotes the value of $\mathbf{T}$ at which the enclosed expression is minimized; $\| \cdot \|_p$ denotes L^p norm, the measure of distance; q is the exponent of the norm; $\mathbf{R}_n(\mathbf{T})$ is a penalty; λ_n is a tuning parameter controlling the strength of each penalty. $\mathbf{G} * \mathbf{T} - \mathbf{u}$ is the rearranged form of Eq. (1.4). If $\lambda_n = 0$, there are no penalties, and thus Eq. (3.3) is reduced to the unregularized Eq. (1.4) upon only minimizing $\|\mathbf{G} * \mathbf{T} - \mathbf{u}\|_{p_1}^{q_1}$.

3.2.2 The effect of L^p norm

One crucial concept in regularization is the measure of distance, L^p norm. Independent of the dimensionality, p sets the standard of the measure of distance, where the different p give different lengths of a vector. Roughly, the L^p norm of a 2D vector $\mathbf{d} = (d_1, d_2)$:

$$\|\mathbf{d}\|_p = (|d_1|^p + |d_2|^p)^{\frac{1}{p}}, \quad p > 0 \tag{3.4}$$

where $| \cdot |$ denotes absolute value. The effect of p in practice can be understood from the contour line of the norm of $\mathbf{d}$. A contour line is a curve along which a value is constant. On a topographic contour map, each contour line marks the location of a constant altitude. On a meteorological pressure contour map, each contour line marks the location of a constant pressure. Similarly for L^p norm, each contour line marks the end points of the vectors of a

constant length. The contour lines shape differently for different p. The most recognizable case is L^2 norm in 2D:

$$\|\mathbf{d}\|_2 = \sqrt{d_1^2 + d_2^2} \tag{3.5}$$

In this case, the contour lines are circles. However, with L^1 norm in 2D:

$$\|\mathbf{d}\|_1 = |d_1| + |d_2| \tag{3.6}$$

the contour line are squares with the vertices on the axes. Notably, the transformation of a vector, such as $\mathbf{G} * \mathbf{T} - \mathbf{u}$ and $\mathbf{R}_n(\mathbf{T})$ for $\mathbf{T}$ in Eq. (3.3), makes a vector function and can change the shape, scale, and location of the contour line. Therefore, the contour line of the norm of a vector function may have a different shape, scale, and location from that of the vector itself. Dissimilarly, the power of the norm, such as $\|\mathbf{G} * \mathbf{T} - \mathbf{u}\|_{p_1}^{q_1}$ and $\|\mathbf{R}_n(\mathbf{T})\|_{p_2}^{q_2}$ in Eq. (3.3), only changes the scale of the contour line, but not the shape and location.

Minimizing a norm is like travelling towards the bottom of a basin or the low-pressure centre of an area – an explorer starts at an arbitrary place and heads across the contour lines towards the centre of the curves. In optimization problems like Eq. (3.3), several norms are to be minimized – the explorer treks to the place with the altogether lowest altitude, pressure, and perhaps other measurements. Each norm or measurement has its own set of concentric contour lines, the centre of which is the minimum for each. However, the overall contour lines would be the superposition of the individual sets of the contour lines.

The overall minimum would not be at the centre of any individual set of contour lines, but somewhere amongst those centres. In Eq. (3.3), $\mathbf{T}$ would be the location of the explorer, and $\|\mathbf{G}*\mathbf{T}-\mathbf{u}\|_{p_1}^{q_1}$ and $\|\mathbf{R}_n(\mathbf{T})\|_{p_2}^{q_2}$ are the different measurements. T of the overall minimum is at the centre of the superimposed contour lines of $\|\mathbf{G}*\mathbf{T}-\mathbf{u}\|_{p_1}^{q_1}$ and $\|\mathbf{R}_n(\mathbf{T})\|_{p_2}^{q_2}$.

Expectedly, the location of the overall minimum is affected by the shape of each individual set of contour lines. For each set, while the norm is constant on each contour line despite the shape, a location along the line nearer to convex vertices is "farther" from the centre of the line and therefore possibly "closer" to the centres of other contour lines. Accordingly, at such a location, the norms with respect to other individual sets of contour lines is likely to be smaller. In other words, on a contour line in an individual set, the overall norm at a location nearer to a vertex is probably smaller. Therefore, the overall minimum is prone to be at or near a vertex of an individual set of contour lines. In this way, p affects the overall minimum by changing the shape of the contour lines of L^p norm. Some values of p promote the minimum to be on or near the vertices. Notably, for $p \leq 1$, the contour lines have vertices on the axes. A point on or near an axis has the other axis component equal or close to zero. Hence, the contour lines with vertices on axes induce zero or sparsity in the minimum.

The 2D case above may appear to indicate that $L^p, p \leq 1$, norm promotes only one non-zero value. This apparent property does not align with the reality of TFM that multiple non-zero vectors exist in the traction field. TFM concerns vector fields. A vector field,

such as $\mathbf{u}$, $\mathbf{T}$, and $\mathbf{G}$, can be reshaped into a single column, becoming a n-D vector with n dependent on the size of the field. Therefore, in TFM, all the 2D vectors add up to very high dimensionality. The generalization from 2D to 3D provides intuition on the high-dimensional case of TFM. In 3D, the terminal of vectors of a norm are on an isosurface instead of a contour line. The isosurfaces with vertices on axes shape similarly to octahedrons that would be formed by the L^1 norm of a vector. For such an isosurface, a location nearer to vertices and edges is "farther" from the centre of the isosurface and possibly "closer" to the centres of other isosurfaces. Hence, the overall minimum is prone to be at or near a vertex or edge of an individual set of isosurfaces. Like the 2D case, a point around a vertex has the other two axis components close to zero. A point around an edge has one axis component close to zero. Therefore, isosurfaces with vertices on axes also induce zero or sparsity in the minimum.

As mentioned above, all the 2D vectors add up to very high dimensionality in TFM. The L^p norm of a n-D vector $\mathbf{d} = (d_1, d_2, \cdots, d_n)$ is roughly defined as:

$$\|\mathbf{d}\|_p = \left(\sum_{i=0}^{n} |d_i|^p\right)^{\frac{1}{p}} = (|d_1|^p + |d_2|^p + \cdots + |d_n|^p)^{\frac{1}{p}}, \quad p > 0 \tag{3.7}$$

Given the same $\mathbf{d}$, different p give different lengths of $\mathbf{d}$, $\|\mathbf{d}\|_p$. Conventionally, the measure

of $p = 2$, the L^2 norm or Euclidean distance, is used:

$$\|\mathbf{d}\|_2 = \left(\sum_{i=0}^{n} |d_i|^2\right)^{\frac{1}{2}} = \sqrt{d_1^2 + d_2^2 + \cdots + d_n^2} \tag{3.8}$$

Therefore, $\|\mathbf{G} * \mathbf{T} - \mathbf{u}\|_2$, the L^2 norm of the difference between the vectors in $\mathbf{G} * \mathbf{T}$ and $\mathbf{u}$, is usually used in Eq. (3.3). Measures other than $p = 2$, such as the L^1 norm:

$$\|\mathbf{d}\|_1 = \sum_{i=0}^{n} |d_i| = |d_1| + |d_2| + \cdots + |d_n| \tag{3.9}$$

are more applicable to the penalties, $\mathbf{R}_n(\mathbf{T})$.

3.2.3 The common techniques

Generally, three types of regularization techniques have been used in TFM. First, for the assumption that the traction is sparse, or in other words, only non-zero at some spots assuming to be focal adhesions, $L^p, p \leq 1$, regularization can be used because it induces sparsity [Fu 1998; Tibshirani 1996]. Due to the computational difficulty in solving the optimization problem for $p < 1$, L^1 regularization is employed for convenience [Ge et al. 2011]:

$$\underset{\mathbf{T}}{\operatorname{argmin}} \left[\|\mathbf{G} * \mathbf{T} - \mathbf{u}\|_2^2 + \lambda \|\mathbf{T}\|_1\right] \tag{3.10}$$

Under L^1 regularization, the $\mathbf{T}$ at the minimum of Eq. (3.10) are prone to contains zeros, resulting in a sparse solution. Additionally, L^1 regularization is also used to solve underdetermined linear systems. Because the majority of the solution is encouraged to be zero by L^1 regularization, this regularization effectively promotes solving for only the remaining non-zero values [Donoho 2006]. Therefore, under L^1 regularization, sparse traction at higher resolution can be reconstructed from displacement at lower resolution [Brask et al. 2015; Han et al. 2015; Suñe-Auñón et al. 2016]. Second, Tikhonov regularization addresses the smoothness of the solution and can be used based on the assumption about the smoothness of the traction. Tikhonov regularization takes the general form of:

$$\underset{\mathbf{T}}{\operatorname{argmin}} \left[\|\mathbf{G} * \mathbf{T} - \mathbf{u}\|_2^2 + \lambda \|\mathbf{\Gamma T}\|_2^2 \right] \tag{3.11}$$

where $\mathbf{\Gamma}$ is a matrix operator specific to a measure of smoothness [Tikhonov et al. 1995]. For example, a first-derivative operator addresses uniformness, and a second-derivative operator addresses curvature. Commonly in TFM, $\mathbf{\Gamma}$ is an identity matrix and the regularization is therefore a zeroth-order Tikhonov regularization, also known as L^2 regularization [Tikhonov et al. 1995]. Particularly, while L^2 regularization does not induce sparsity, this method does assume the distribution of the traction values to be Gaussian. Higher orders of Tikhonov regularization addressing different measures of smoothness is rarely used because the traction field is not assumed to be smooth under those measures [Balaban et al. 2001]. Third, as the noise have apparent distinctively high frequencies, low-pass filtering can be used to

truncate the displacement in the frequency domain, directly removing the high-frequency components in the displacement and smoothing the data [Tanimoto and Sano 2012]. The cutoff frequency determines the strength of regularization. The choice of regularization technique is not restricted to the above three. Alternative suitable regularization techniques are also available, such as truncated SVD and proximal gradient methods [Hansen 2010; Huang et al. 2019]. Different regularization techniques can be combined as in Eq. (3.3) [Huang et al. 2019].

Given a dataset, because L^2 regularization, low-pass filtering, and L^1 regularization only account for arbitrary measures of smoothness and sparsity, any of these techniques can be better than another. L^2 regularization and low-pass filtering have been popular as regularization techniques in general, so there is no surprise that these methods have been broadly used in TFM as well. However, recently L^1 regularization was demonstrated to outperform the alternatives in many cases [Colin-York et al. 2016; Sabass et al. 2008; Schwarz et al. 2002; Suñe-Auñón et al. 2017]. Convenient as such comparison may appear, attention should be drawn to the experimental condition under which the conclusion is made, as the assumptions thereof can strongly affect the traction calculation. Do the traction values have a Gaussian distribution? Is the traction field sparse? Are the noise and artifacts separable in the frequency domain? Particularly, there is no strict definition regarding the ratio between the number of non-zero and zero values for the traction to qualify as sparse. However, a reasonable initial conjecture would be, for example, that the

traction is sparse and thus L^1 regularization valid for single cell experiments, but not so for monolayer experiments. Because single cell images zoom in to one cell in which the focal adhesions only occupy a small portion of the cell area, the non-zero-to-zero ratio of traction is low. On the contrary, monolayers images zoom out to larger scales on which the cells and therefore focal adhesions can become densely located in the image, so the non-zero-to-zero ratio of traction is high. Accordingly, the best regularization technique(s) depends on the properties of that specific displacement data and the underlying traction.

A suitable regularization technique alone cannot guarantee an accurate solution. The tuning parameter λ_n and the cutoff frequency for low-pass filtering determine the strength of regularization and therefore also the accuracy of the solution. Overly small λ_n and high cutoff frequency do not regularize the solution sufficiently, leaving the remaining effect of the noise in the traction. Excessively large λ_n and low cutoff frequency result in oversimplified solution, abating the actual displacement. A variety of methods to determine the strength of regularization are well-developed, including L-curve criterion, discrepancy principle, self-consistence criterion, and more recently, Bayesian methods [Engl 1987; Golberg 1979; Hansen 2007; Honerkamp and Weese 1990; Huang et al. 2019].

3.3 Remarks on DL methodologies

The outcome of experimenting with time span and time resolution in DeepMorphoTM aligns with the quasi-static nature of cell deformation and locomotion. This property may reduce

the necessity of adopting the Recurrent Neural Networks (RNNs) for processing cellular dynamics, justifying the use of CNNs in DeepMorphoTM. However, the performance of RNNs and CNNs on modeling cellular dynamics needs to be quantified to reach a conclusion, as the quasi-static property is implied in hindsight by CNNs.

While no accurate analytical model of cell contractility is established, fundamental physical laws governing cell contractility are known. Properties of cell contractility have also been discovered and can be modeled analytically, such as the quasi-static nature, viscous energy dissipation, and underdamped wave-like fluctuations [Bastounis et al. 2011; Ghabache et al. 2021; Inagaki and Katsuno 2017]. To promote interpretability, generalizability, and potentially performance, NNs can be integrated with these known equations and equation solvers in latent and data space, yielding a partially parameterized model. While DeepMorphoTM did not explore this direction, leveraging known equations is fundamental to modeling physics with DL.

DeepMorphoTM avoids the ill-posedness by directly inferring substrate displacement rather than cell traction. The small amount of noise in the displacement measurement does not significantly affect learning and is neither learnt nor inferred unless NNs overfit. Prior to this design, alternatives have been experimented. Using the unregularized ground truth traction, the direct inference of the traction was attempted through employing regularization techniques for DL training, such as weight decay and batch normalization. However, good training quality could not be achieved due to heavy noise in the ground truth. Another option

is to directly infer the traction, compute the displacement through the forward computation of Eq. 1.4, and make only the displacement target in training. Additional loss terms, such as net momentum, were also experimented. However, none of the alternatives produced any significant effect. Therefore, although sophisticated methodologies are tempting, such methodologies are futile unless they address the data properly.

Chapter 4

Conclusion and future work

This thesis demonstrates the significance of a comprehensive understanding of a system and data to modeling a physical system with DL. The mechanical system of a cell and its underlying substrate is modeled with DeepMorphoTM based on experimentally measured cell shapes. DeepMorphoTM accurately infers effective ensemble-average substrate displacement from a shape sequence of a cell with a CNN and subsequently computes cell traction, offering a simpler and more robust alternative to TFM. The mathematics, mechanics, biology, and algorithms behind TFM and cell contractility are studied, and DL methodologies are designed accordingly. For both training and inference, the ill-posedness in the computation of traction is circumvented by the absence of high-frequency noise in the inferred displacement. Moreover, DeepMorphoTM reveals information beyond TFM analysis, suggesting common mechanics underlying cell contractility, viscous energy

dissipation in cell deformation and locomotion, and the quasi-static nature of biological processes. Notably, while this thesis does not investigate the integration of NNs with known equations and equation solvers in a latent or data space, this direction is crucial to modeling physics with DL for interpretability, generalizability, and performance.

Future research delves into the integration of equations and differentiable solvers in, particularly, a latent space. Often, complex high-dimensional systems have simple low-dimensional behaviour in an appropriate basis which can be defined by fundamental physical relationships. DL provides great flexibility in the shaping of a latent space where this basis may exist. The general goal of future works is to map between a high-dimensional system space and a low-dimensional latent space manifesting simple latent physics; in this way, high-dimensional complex simulations can be performed through the latent space with stability and low cost. Major challenges include the smoothness of the latent space in space and time, the interpretability and, potentially, disentanglement of the latent dimensions, and the fidelity of the reconstruction from the latent space.

Beyond the scope of this thesis, this future direction was attempted without success in the experimental case of cell contractility. The attempt was too ambitious due to the lack of an established mechanical model for the biological system and the complexity of experimentally acquired data. Therefore, future studies start from established systems and simulated data.

Bibliography

Ronald J Adrian. Scattering particle characteristics and their effect on pulsed laser measurements of fluid flow: speckle velocimetry vs particle image velocimetry. *Appl. Opt.*, 23(11):1690–1691, 1984. doi: 10.1364/AO.23.001690.

Nathalie Q Balaban, Ulrich S Schwarz, Daniel Riveline, Polina Goichberg, Gila Tzur, Ilana Sabanay, Diana Mahalu, Sam Safran, Alexander Bershadsky, and Lia Addadi. Force and focal adhesion assembly: a close relationship studied using elastic micropatterned substrates. *Nature cell biology*, 3(5):466–472, 2001.

Rachid Berair, Florence Hollins, and Christopher Brightling. Airway smooth muscle hypercontractility in asthma. *Journal of Allergy*, 2013:185971, 2013. doi: 10.1155/2013/185971.

Joseph Boussinesq. *Application des potentiels à l'étude de l'équilibre et du mouvement des solides élastiques: principalement au calcul des déformations et des pressions que produisent, dans ces solides, des efforts quelconques exercés sur une petite partie de leur*

surface ou de leur intérieur: mémoire suivi de notes étendues sur divers points de physique, mathematique et d'analyse. Gauthier-Villars, 1885.

Jonatan B Brask, Guillem Singla-Buxarrais, Marina Uroz, Romaric Vincent, and Xavier Trepat. Compressed sensing traction force microscopy. *Acta Biomaterialia*, 26:286–294, 2015. doi: 10.1016/j.actbio.2015.08.023.

James P Butler, Iva M Tolić-Nørrelykke, Ben Fabry, and Jeffrey J Fredberg. Traction fields, moments, and strain energy that cells exert on their surroundings. *American Journal of Physiology-Cell Physiology*, 282(3):C595–C605, Mar 2002. doi: 10.1152/ajpcell.00270.2001.

Ferdous Chowdhury, Billy Huang, and Ning Wang. Cytoskeletal prestress: The cellular hallmark in mechanobiology and mechanomedicine. *Cytoskeleton*, 78(6):249–276, 2021. doi: https://doi.org/10.1002/cm.21658.

Huw Colin-York, Dilip Shrestha, James H Felce, Dominic Waithe, Emad Moeendarbary, Simon J Davis, Christian Eggeling, and Marco Fritzsche. Super-resolved traction force microscopy (stfm). *Nano letters*, 16(4):2633–2638, 2016.

L M Delves and J L Mohamed. *Computational methods for integral equations*. CUP Archive, 1988.

Micah Dembo and Yu-li Wang. Stresses at the cell-to-substrate interface during locomotion of

fibroblasts. *Biophysical Journal*, 76(4):2307–2316, Apr 1999. doi: 10.1016/S0006-3495(99)77386-8.

David L Donoho. Compressed sensing. *IEEE Transactions on Information Theory*, 52(4):1289–1306, 2006. doi: 10.1109/TIT.2006.871582.

Bryant L Doss, Meng Pan, Mukund Gupta, Gianluca Grenci, René-Marc Mège, Chwee Teck Lim, Michael P Sheetz, Raphaël Voituriez, and Benoît Ladoux. Cell response to substrate rigidity is regulated by active and passive cytoskeletal stress. *Proceedings of the National Academy of Sciences*, 117(23):12817–12825, 2020.

Christopher C DuFort, Matthew J Paszek, and Valerie M Weaver. Balancing forces: architectural control of mechanotransduction. *Nature Reviews Molecular Cell Biology*, 12(5):308–319, 2011. doi: 10.1038/nrm3112.

Kyle L Ellefsen, Jesse R Holt, Alice C Chang, Jamison L Nourse, Janahan Arulmoli, Armen H Mekhdjian, Hamid Abuwarda, Francesco Tombola, Lisa A Flanagan, Alexander R Dunn, et al. Myosin-ii mediated traction forces evoke localized piezo1-dependent ca2+ flickers. *Communications biology*, 2(1):298, 2019.

Alberto Elosegui-Artola, Ion Andreu, Amy EM Beedle, Ainhoa Lezamiz, Marina Uroz, Anita J Kosmalska, Roger Oria, Jenny Z Kechagia, Palma Rico-Lastres, Anabel-Lise Le Roux, et al. Force triggers yap nuclear entry by regulating transport across nuclear pores. *Cell*, 171(6):1397–1410, 2017.

Heinz Werner Engl. Discrepancy principles for tikhonov regularization of ill-posed problems leading to optimal convergence rates. *Journal of Optimization Theory and Applications*, 52(2):209–215, Feb 1987. doi: 10.1007/BF00941281.

Wenjiang J Fu. Penalized regressions: the bridge versus the lasso. *Journal of Computational and Graphical Statistics*, 7(3):397–416, 1998. doi: 10.2307/1390712.

Ding-Xuan Ge, Xuejun Jiang, and Yinyu Ye. A note on the complexity of lp minimization. *Mathematical Programming*, 129(2):285–299, Oct 2011. doi: 10.1007/s10107-011-0470-2.

MA Golberg. *Solution methods for integral equations*. Springer, 1979.

Jacques Hadamard. On problems with partial derivatives and their physical meaning. *Princeton university bulletin*, pages 49–52, 1902.

Jacques Hadamard. *Lectures on Cauchy's problem in linear partial differential equations*. Courier Corporation, 2003.

Sang-Joon Han, Yeonho Oak, Alex Groisman, and Gaudenz Danuser. Traction microscopy to identify force modulation in subresolution adhesions. *Nature methods*, 12(7):653–656, 2015. doi: 10.1038/nmeth.3430.

Per Christian Hansen. Regularization tools version 4.0 for matlab 7.3. *Numerical Algorithms*, 46(2):189–194, Oct 2007. doi: 10.1007/s11075-007-9136-9.

Per Christian Hansen. *Discrete inverse problems: insight and algorithms*. SIAM, 2010.

Alan K Harris, Peter Wild, and David Stopak. Silicone rubber substrata: a new wrinkle in the study of cell locomotion. *Science*, 208(4440):177–179, 1980.

Johann Honerkamp and Joachim Weese. Tikhonov's regularization method for ill-posed problems. *Continuum Mechanics and Thermodynamics*, 2(1):17–30, Mar 1990. doi: 10.1007/BF01170953.

Jianyong Huang, Xiaoling Peng, Lei Qin, Tao Zhu, Chunyang Xiong, Youyi Zhang, and Jing Fang. Determination of cellular tractions on elastic substrate based on an integral boussinesq solution. 2009.

Yunfei Huang, Christoph Schell, Tobias B Huber, Ahmet Nihat Şimşek, Nils Hersch, Rudolf Merkel, Gerhard Gompper, and Benedikt Sabass. Traction force microscopy with optimized regularization and automated bayesian parameter selection for comparing cells. *Scientific reports*, 9(1):1–16, 2019.

Sung Sik Hur, Ying Zhao, Yun-Soung Li, Elliot Botvinick, and Shu Chien. Live cells exert 3-dimensional traction forces on their substrata. *Cellular and Molecular Bioengineering*, 2(3):425–436, Sep 2009. doi: 10.1007/s12195-009-0082-6.

Sung Sik Hur, Juan C Del Alamo, Joon Seok Park, Yi-Shuan Li, Hong A Nguyen, Dayu Teng, Kuei-Chun Wang, Leona Flores, Baldomero Alonso-Latorre, Juan C Lasheras, et al. Roles of cell confluency and fluid shear in 3-dimensional intracellular forces in endothelial cells. *Proceedings of the National Academy of Sciences*, 109(28):11110–11115, 2012.

Richard D Keane and Ronald J Adrian. Theory of cross-correlation analysis of piv images. In Frans TM Nieuwstadt, editor, *Flow Visualization and Image Analysis*, pages 1–25. Springer Netherlands, 1993.

Rainer Kress, Vladimir Maz'ya, and Vladimir Kozlov. *Linear integral equations*. Springer, 1989.

Sanjay Kumar and Valerie M Weaver. Mechanics, malignancy, and metastasis: the force journey of a tumor cell. *Cancer Metastasis Reviews*, 28(1-2):113–127, Jun 2009. doi: 10.1007/s10555-008-9173-4.

L D Landau and E M Lifshitz. *Theory of elasticity*, volume 7. Pergamon Press, Oxford New York, 1986.

Jennifer Lee, Marc Leonard, Tim Oliver, Akira Ishihara, and Ken Jacobson. Traction forces generated by locomoting keratocytes. *J Cell Biol*, 127(6):1957–1964, 1994.

Wesley R Legant, Jordan S Miller, Brian L Blakely, Daniel M Cohen, Guy M Genin, and Christopher S Chen. Measurement of mechanical tractions exerted by cells in three-dimensional matrices. *Nature methods*, 7(12):969, 2010.

Arthur Lesman, Jacob Notbohm, David A Tirrell, and Guruswami Ravichandran. Contractile forces regulate cell division in three-dimensional environments. *Journal of Cell Biology*, 205(2):155–162, 2014. doi: 10.1083/jcb.201309029.

Bin Li and James H-C Wang. Fibroblasts and myofibroblasts in wound healing: force generation and measurement. *J Tissue Viability*, 20(4):108–20, Nov 2011. doi: 10.1016/j.jtv.2009.11.004.

Sarah A Maskarinec, Christian Franck, David A Tirrell, and Guruswami Ravichandran. Quantifying cellular traction forces in three dimensions. *Proceedings of the National Academy of Sciences*, 106(52):22108–22113, 2009. doi: 10.1073/pnas.0904565106.

Hossein Mesgarani and Yaser Azari. Numerical investigation of fredholm integral equation of the first kind with noisy data. *Mathematical Sciences*, 13(3):267–278, 2019. doi: 10.1007/s40096-019-00296-7.

Juliane Münch and Salim Abdelilah-Seyfried. Sensing and responding of cardiomyocytes to changes of tissue stiffness in the diseased heart. *Front Cell Dev Biol*, 9:642840, 2021. doi: 10.3389/fcell.2021.642840.

Jacob Notbohm, Jin H Kim, Anand R Asthagiri, and Guruswami Ravichandran. Three-dimensional analysis of the effect of epidermal growth factor on cell-cell adhesion in epithelial cell clusters. *Biophysical Journal*, 102(6):1323–1330, 2012. doi: 10.1016/j.bpj.2012.02.016.

Francesco S Pasqualini, Ashutosh Agarwal, Brendan B O'Connor, Qiaobing Liu, Sean P Sheehy, and Kevin KK Parker. Traction force microscopy of engineered cardiac tissues. *PLoS One*, 13(3):e0194706, 2018. doi: 10.1371/journal.pone.0194706.

Markus Raffel, Christian E Willert, and Jürgen Kompenhans. *Particle image velocimetry: a practical guide*. Springer, 1998.

Sumati Ram-Mohan, Yan Bai, Niccole Schaible, Allen J Ehrlicher, Daniel P Cook, Bela Suki, David A Stoltz, Julian Solway, Xingbin Ai, and Ramaswamy Krishnan. Tissue traction microscopy to quantify muscle contraction within precision-cut lung slices. *American Journal of Physiology-Lung Cellular and Molecular Physiology*, 318(2):L323–L330, 2020.

Benedikt Sabass, Margaret L Gardel, Clare M Waterman, and Ulrich S Schwarz. High resolution traction force microscopy based on experimental and computational advances. *Biophysical journal*, 94(1):207–220, 2008. doi: 10.1529/biophysj.107.113670.

Ulrich S Schwarz and Jérôme RD Soiné. Traction force microscopy on soft elastic substrates: A guide to recent computational advances. *Biochimica et Biophysica Acta (BBA)-Molecular Cell Research*, 1853(11):3095–3104, 2015. doi: 10.1016/j.bbamcr.2015.05.028.

Ulrich S Schwarz, Nathalie Q Balaban, Daniel Riveline, Alexander Bershadsky, Benjamin Geiger, and Samuel A Safran. Calculation of forces at focal adhesions from elastic substrate data: the effect of localized force and the need for regularization. *Biophysical Journal*, 83 (3):1380–1394, 2002. doi: 10.1016/S0006-3495(02)73909-X.

Eize Stamhuis and John Videler. Quantitative flow analysis around aquatic animals using laser sheet particle image velocimetry. *Journal of Experimental Biology*, 198(2):283–294, 1995. doi: 10.1242/jeb.198.2.283.

Alberto Suñe-Auñón, Alvaro Jorge-Peñas, Hans Van Oosterwyck, and Arrate Muñoz-Barrutia. L1-regularized reconstruction for traction force microscopy. In *2016 IEEE 13th International Symposium on Biomedical Imaging (ISBI)*, pages 140–144, 2016. doi: 10.1109/ISBI.2016.7493230.

Alberto Suñe-Auñón, Alvaro Jorge-Peñas, Rocio Aguilar-Cuenca, Miguel Vicente-Manzanares, Hans Van Oosterwyck, and Arrate Muñoz-Barrutia. Full l1-regularized traction force microscopy over whole cells. *BMC Bioinformatics*, 18(1):365, 2017. doi: 10.1186/s12859-017-1771-0.

Jolene L Tan, Joe Tien, Dana M Pirone, Douglas S Gray, Kiran Bhadriraju, and Christopher S Chen. Cells lying on a bed of microneedles: an approach to isolate mechanical force. *Proc Natl Acad Sci U S A*, 100(4):1484–1489, 2003. doi: 10.1073/pnas.0235407100.

Neetu Taneja, Lindsay Rathbun, Heidi Hehnly, and Dylan T Burnette. The balance between adhesion and contraction during cell division. *Curr Opin Cell Biol*, 56:45–52, Feb 2019. doi: 10.1016/j.ceb.2018.09.001.

Hirokazu Tanimoto and Masakiyo Sano. Dynamics of traction stress field during cell division. *Physical Review Letters*, 109(24):248110, 2012. doi: 10.1103/PhysRevLett.109.248110.

Robert Tibshirani. Regression shrinkage and selection via the lasso. *Journal of the Royal*

Statistical Society. Series B (Methodological), 58(1):267–288, 1996. URL `http://www.jstor.org/stable/2346178`.

Anatoliĭ N Tikhonov, Anatolii Goncharsky, Valeriĭ Stepanov, and Andrey G Yagola. *Numerical methods for the solution of ill-posed problems*. Springer Science & Business Media, 1995.

Jennet Toyjanova, Eyal Bar-Kochba, Cristina López-Fagundo, Jonathan Reichner, Diane Hoffman-Kim, and Christian Franck. High resolution, large deformation 3d traction force microscopy. *PLOS ONE*, 9(4):e90976, 2014. doi: 10.1371/journal.pone.0090976.

F Ursell. Introduction to the theory of linear integral equations. In L M Delves and J Walsh, editors, *Numerical solution of integral equations*, pages 2–11. Oxford: Clarendon Press, 1974.

Christian E Willert and Morteza Gharib. Digital particle image velocimetry. *Experiments in Fluids*, 10(4):181–193, 1991. doi: 10.1007/BF00190388.

Evelyn KF Yim and Michael P Sheetz. Force-dependent cell signaling in stem cell differentiation. *Stem Cell Research & Therapy*, 3(5):41, 2012. doi: 10.1186/scrt132.